



HAL
open science

To stick or to slip: A reset PID control perspective on positioning systems with friction

A. Bisoffi, R. Beerens, W.P.M.H. Heemels, H. Nijmeijer, N. van de Wouw,
Luca Zaccarian

► To cite this version:

A. Bisoffi, R. Beerens, W.P.M.H. Heemels, H. Nijmeijer, N. van de Wouw, et al.. To stick or to slip: A reset PID control perspective on positioning systems with friction. *Annual Reviews in Control*, 2020, 49, pp.37-63. 10.1016/j.arcontrol.2020.04.010 . hal-03029046

HAL Id: hal-03029046

<https://hal.science/hal-03029046v1>

Submitted on 27 Nov 2020

HAL is a multi-disciplinary open access archive for the deposit and dissemination of scientific research documents, whether they are published or not. The documents may come from teaching and research institutions in France or abroad, or from public or private research centers.

L'archive ouverte pluridisciplinaire **HAL**, est destinée au dépôt et à la diffusion de documents scientifiques de niveau recherche, publiés ou non, émanant des établissements d'enseignement et de recherche français ou étrangers, des laboratoires publics ou privés.

To stick or to slip: A reset PID control perspective on positioning systems with friction

A. Bisoffi^b, R. Beerens^a, W.P.M.H. Heemels^a, H. Nijmeijer^a, N. van de Wouw^{a,c}, L. Zaccarian^{d,e,*}

^a*Eindhoven University of Technology, Department of Mechanical Engineering, P.O. Box 513, 5600MB Eindhoven, The Netherlands*

^b*ENTEG and the J.C. Willems Center for Systems and Control, University of Groningen, 9747 AG Groningen, The Netherlands*

^c*University of Minnesota, Civil, Environmental & Geo-Engineering Department, MN 55455, USA.*

^d*CNRS, LAAS, Université de Toulouse, 31400 Toulouse, France*

^e*Dipartimento di Ingegneria Industriale, University of Trento, 38123 Trento, Italy*

Abstract

We overview a recent research activity where suitable reset actions induce stability and performance of PID-controlled positioning systems suffering from nonlinear frictional effects. With a Coulomb-only effect, PID feedback produces a set of equilibria whose asymptotic (but not exponential) stability can be certified by using a discontinuous Lyapunov-like function. With velocity weakening effects (the so-called Stribeck friction), the set of equilibria becomes unstable with PID feedback and the so-called “hunting phenomenon” (persistent oscillations) is experienced. Resetting laws can be used in both scenarios. With Coulomb friction only, the discontinuous Lyapunov-like function immediately suggests a reset action providing extreme performance improvement, preserving stability and inducing desirable exponential convergence of a relevant subset of the solutions. With Stribeck, a more sophisticated set of logic-based reset rules recovers global asymptotic stability of the set of equilibria, providing an effective solution to the hunting instability. We clarify here the main steps of the Lyapunov-based proofs associated to our reset-enhanced PID controllers. These proofs involve building semiglobal hybrid representations of the solutions in the form of hybrid automata whose logical variables enable transforming the aforementioned discontinuous function into smooth or at least Lipschitz ones. Our theoretical results are illustrated by extensive simulations and experimental validation on an industrial nano-positioning system.

Keywords: stick and slip, Coulomb friction, Stribeck friction, positioning system, reset control, hybrid automata, mechatronic application, Lyapunov results

1. Introduction

Setpoint control of motion systems with friction has been an active field of research for the past thirty years because of its relevance in an abundance of applications, such as electron microscopy, robotics, pick-and-place machines, printers, semiconductor equipment and many more. As friction limits the system’s performance in terms of, e.g., achievable accuracy and speed, many different control solutions have been developed. These control solutions can be roughly divided into two groups, namely, model-based friction compensation techniques and non-model-based control techniques.

Model-based compensation techniques rely on developing as-accurate-as-possible friction models, which are used in a control loop to compensate friction and, hence, to counteract its detrimental effects. Early friction models

date back as far the sixteenth century, where Amontons and Coulomb [6] proposed the first static friction models. Morin [59] showed that, at zero velocity, the friction force balances with the external forces applied to the system where static friction may be larger than Coulomb friction (which has led eventually to the mathematical *set-valued* description of static friction, see, e.g., [51]). In 1902, Stribeck showed a continuous, velocity-dependent decrease from static to Coulomb friction levels [76], commonly present in lubricated contacts and widely known as the *Stribeck* effect. Further developments have led to dynamic friction models to accommodate for *presliding* effects (see, e.g., [5, 74]), such as the Dahl model [32], the LuGre model [26], or the ones in [77, 4].

These models are used for friction compensation in, e.g., [11, 39, 54, 55], or for controller synthesis in [73, 3]. However, model-based control techniques which use the above friction models in their design are prone to model mismatches, since friction often varies due to, e.g., changing ambient or lubrication conditions or wear. Model mismatch leads to over- or under-compensation of friction, so that the system may exhibit limit cycles or nonzero steady-state errors (compromising the positioning accu-

*Corresponding author

¹*Email addresses:* {r.beerens; m.heemels; h.nijmeijer; n.v.d.wouw}@tue.nl, a.bisoffi@rug.nl, zaccarian@laas.fr. This work is part of the research programme CHAMeleon with project number 13896, which is (partly) financed by the Netherlands Organisation for Scientific Research (NWO). Research supported in part by ANR via grant HANDY, number ANR-18-CE40-0010.

rary), as thoroughly analyzed in [72]. In order to obtain some robustness to changing frictional conditions, model-based compensation methods are enhanced with parameter adaptation techniques in, e.g., [7, 28, 60]. However, mismatches in the model structure (and hence the associated performance limitations) still remain.

Non-model-based control techniques do not rely on on-line friction compensation, but on applying specific control signals that cope with the apparent friction to achieve the desired performance. Dithering techniques apply a persistent high-frequency control signal to the system to smoothen out the discontinuity induced by Coulomb friction, see, e.g., [48, 67, 81]. Impulsive control applies a carefully determined impulsive control signal so that the system escapes the stick phases with a nonzero position error, see, e.g., [64, 85], and [82]. In [82], finite-time stability of the setpoint is shown. Second-order sliding mode has been applied for setpoint control of systems with friction in [14, 13]. Once the sliding surface is reached, the setpoint is approached from one side (i.e., the velocity does not change sign), rendering the Coulomb friction a constant disturbance and exponential convergence is shown. State feedback control techniques have been explored in [33] to stabilize constant (non-zero) velocity references for systems with a motor-load structure. The controller design is based on a Popov-like criterion for systems with set-valued nonlinearities. Although persistent oscillations in the *velocity* are shown to be effectively suppressed, the proposed technique is not a solution for the *setpoint regulation* control problem that we consider in this work.

Despite the existence of the above control techniques, classical proportional-integral-derivative (PID) controllers are still commonly used for the positioning of frictional motion systems in the industry. With PID solutions, the integrator action is capable of compensating for unknown static friction values by building up control force while integrating the position error. However, PID control has some performance limitations as well. First, convergence is slow for PID-controlled systems with Coulomb friction. The integrator action is required to escape the stick phase by building up enough control force. If the solution overshoots the setpoint in the resulting slip phase, however, the control signal must point in the opposite direction to overcome the static friction again. This process takes increasingly more time with a decreasing position error, resulting in slow convergence that adversely affects the machine throughput. Secondly, the integrator action in the presence of the velocity-weakening (Stribeck) effect induces persistent oscillations (the so-called *hunting phenomenon*), jeopardizing the achievable accuracy [11, 46, 55].

In order to address the limitations of PID control for frictional systems, we propose here the use of *reset* enhancements that can serve as an add-on to the classical PID controller. Reset controllers were first proposed 50 years ago by [31], with the goal of providing more flexibility in linear controller designs and at potentially removing fundamental performance limitations of linear controllers.

The first systematic designs for reset controllers were reported in the 1970's by [49, 47] who introduced the so-called First Order Reset Element (FORE). There has been a renewed interest in this class of systems after the late 1990's (see [20] and references therein).

In the past decade or so, reset controllers were addressed using the hybrid systems framework of [41], thus providing Lyapunov-based conditions for \mathcal{L}_2 stability and exponential stability of reset systems possibly including an exponentially unstable FORE [62, 86, 61]. Paralleling these works, the scientific community has addressed in multiple ways the goal of generalizing the concept of reset systems to broader classes of controllers reaching beyond classical control solutions. Some key works with relevant references can be found in [1] where \mathcal{L}_2 and \mathcal{H}_2 properties are investigated, [78] where resets are addressed in a context with saturation, [87] where a generalized first-order reset element (GFORE) has been proposed and characterized, [44] where a lifting approach is used for the case of periodic resets, [88] where a special focus is on the goal of characterizing the performance limitations that can be overcome by reset control, and [84] where frequency-domain tools for stability analysis of reset control system have been proposed. Higher-dimensional generalizations of these reset controllers are proposed in [71] by focusing on a full state feedback architecture and is then generalized, in the context of linear plants, to the case of output feedback and Luenberger observers in [36]. The arising LMI-based conditions, finally led to a state-feedback solution of the \mathcal{H}_∞ design problem in [37] and an output feedback modified version given in the recent paper [35]. Comprehensive overviews of these methods can be found in the monograph [12] and the recent survey paper [70]. Several additional relevant and successful industrial applications of reset control can be found in the literature (see, e.g., [27, 52, 65, 34, 84] and references therein). These applications are mostly focused on performance improvement with *linear* plants. Here we address a more challenging context involving the intrinsic *nonlinear* phenomena associated with frictional systems. In contrast, we consider in this paper the setpoint control problem of PID controlled motion systems with friction, rendering the plant to be controlled essential nonlinear/nonsmooth. We clarify the control problems associated with PID control, and discuss reset control solutions to overcome these limitations.

The results presented in this paper provide a unified and comprehensive overview of the research accomplishments reported in [22, 17, 18, 21, 15] and the preliminary works [16, 19]. As compared to those works we provide here a unified development, highlighting the importance of building hybrid models comprising logic variables to allow for the construction of smooth or Lipschitz Lyapunov functions, in addition to including a novel understanding of the exponential convergence properties of certain solutions in the Coulomb friction case. We also provide a deeper qualitative understanding of the reset closed loop responses, based on extensive simulation resultshighlight-

ing the fact that the net effect of the proposed reset actions is to recover, loosely speaking, the qualitative transient behavior to be expected from the linear responses. As such, a strong advantage of the proposed approach is that it enables retaining the industrial practice on PID gain tuning, making it viable also in the presence of unmodeled frictional effects.

The remainder of this paper is outlined as follows. In Section 2 we discuss the nonlinear dynamics and the peculiar features of the Coulomb and Stribeck cases addressed in this paper, which are then simulated in Section 3, showing the limitations of classical PID designs. Section 4 is devoted to providing a few Lyapunov-based tools that are used throughout the paper and serve as a proof of asymptotic stability for the Coulomb case. Sections 5 and 6 contain the two most important reset strategy presented in our work, the first one addressing the Coulomb case and the second one addressing the Stribeck case. Some experimental validations of the proposed solutions are then reported in Section 7, and Section 8 contains additional illustrations with PID gains tuning that are seldom found in the industrial context. Section 9 concludes the paper and provides some directions of future research.

Notation. Given $x \in \mathbb{R}^n$, $|x|$ is its Euclidean norm. $\text{sign}(\cdot)$ (with a lower-case s) denotes the classical sign function, i.e., $\text{sign}(y) := y/|y|$ for $y \neq 0$ and $\text{sign}(0) := 0$. $\text{Sign}(\cdot)$ (with an upper-case S) denotes the *set-valued* sign function, i.e., $\text{Sign}(y) := \{\text{sign}(y)\}$ for $y \neq 0$, and $\text{Sign}(y) := [-1, 1]$ for $y = 0$. For $c > 0$, the deadzone function $y \mapsto \text{dz}_c(y)$ is defined as: $\text{dz}_c(y) := 0$ if $|y| \leq c$, $\text{dz}_c(y) := y - c\text{sign}(y)$ if $|y| > c$. For column vectors $x_1 \in \mathbb{R}^{d_1}, \dots, x_m \in \mathbb{R}^{d_m}$, the notation (x_1, \dots, x_m) is equivalent to $[x_1^\top \dots x_m^\top]^\top$. \wedge, \vee, \implies denote the logical conjunction, disjunction, implication. A function $f: D \rightarrow \mathbb{R}$ is lower semicontinuous if $\liminf_{x \rightarrow x_0} f(x) \geq f(x_0)$ for each point x_0 in its domain D . The distance of a vector $x \in \mathbb{R}^n$ to a closed set $\mathcal{A} \subset \mathbb{R}^n$ is defined as $|x|_{\mathcal{A}} := \inf_{y \in \mathcal{A}} |x - y|$. $\langle \cdot, \cdot \rangle$ defines the inner product between its two vector arguments.

For a hybrid solution φ [41, Def. 2.6] with hybrid time domain $\text{dom } \varphi$ [41, Def. 2.3], the function $j(\cdot)$ is defined as $j(t) := \min_{(t,k) \in \text{dom } \varphi} k$. Function $j(\cdot)$ depends on the specific solution φ that it addresses, but with a slight abuse of notation we use a unified symbol $j(\cdot)$ because the solution under consideration is always clear from the context. A hybrid solution is maximal if it cannot be extended [41, Def. 2.7], and is complete if its domain is unbounded (in the t - or j -direction) [41, p. 30].

2. Problem formulation

2.1. Plant dynamics and friction model

Consider a point mass m on a horizontal plane described by position s and velocity v , as in Figure 1. The mass is subject to a control input u and a friction force u_f .

The plant dynamics are then given by

$$\dot{s} = v, \quad \dot{v} = \frac{1}{m}(-u_f + u). \quad (1)$$

To represent the friction force u_f acting on the mass, we use a well-known set-valued friction model $v \rightrightarrows \bar{\Psi}(v)$ (the double arrows clarify that $\bar{\Psi}$ may be a set, rather than a single point), which is motivated by many applications including the experimental nano-positioning motion stage discussed in Section 7. For this motion state we measured the particular shape of the experimental pairs (v, u_f) as represented in Figure 2. According to the descriptions in [10, Eq. (3)] or similarly [63, Eq. (5)], the overall friction force u_f represented in Figure 2 is characterized by a two-fold phenomenon:

- *Slip phase.* When the velocity v is nonzero, u_f is uniquely determined by v via three different components comprising a linear viscous friction component $\bar{\alpha}_v v$, a static friction component $\bar{F}_s \text{sign}(v)$, where $\bar{F}_s > 0$ is a positive scalar, and a velocity weakening nonlinear component $\bar{\psi}(v)$ encompassing the so-called Stribeck effect.

- *Stick phase.* When the velocity is (and remains at) zero, causality reverses in the sense that the fact that the system resides in stick (i.e., remains at $v = 0$) imposes the friction force needed to realize such stick condition. Of course, stick can only be maintained if the friction force needed lies in the set $[-\bar{F}_s, \bar{F}_s]$. For the system in Figure 1, this means that u_f is uniquely determined by the force u exerted on the mass and corresponds to the unique selection $u_f \in [-\bar{F}_s, \bar{F}_s]$ in the bounded static friction range $[-\bar{F}_s, \bar{F}_s]$ minimizing the (absolute value of the) net force $u_{\text{net}} = -u_f + u$ acting on the mass.

According to the set-valued friction law [38, p. 53] (or [51, Eqs. (5.36), (5.44)]), an effective way of capturing the above-discussed two-fold mechanism is to characterize friction as a velocity-dependent set-valued map defined as

$$v \rightrightarrows \bar{\Psi}(v) := -\bar{F}_s \text{Sign}(v) - \bar{\alpha}_v v + \bar{\psi}(v), \quad (2)$$

where the function Sign is a set-valued mapping defined as

$$\text{Sign}(v) := \begin{cases} \text{sign}(v), & \text{if } v \neq 0 \\ [-1, 1], & \text{if } v = 0. \end{cases} \quad (3)$$

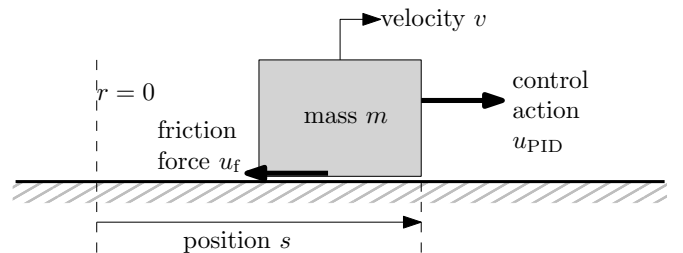


Figure 1: Mass subject to friction and controlled by a PID controller.

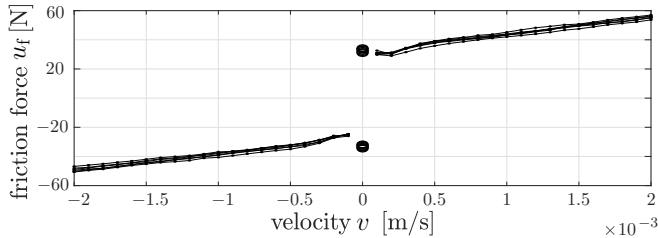


Figure 2: Pairs (v, u_f) measured from the experimental nano-positioning motion stage discussed in Section 7.

Based on the set $\bar{\Psi}(v)$ defined in (2) the model (1) turns into the differential inclusion

$$\dot{s} = v, \quad \dot{v} \in \frac{1}{m}(\bar{\Psi}(v) + u). \quad (4)$$

2.2. Control problem

The presence of friction in motion systems poses major challenges for accurate and fast positioning control. In this paper we consider point-to-point motion and, thus, we focus on the design of a controller such that the resulting closed-loop system has the property that along all solutions the position s is quickly stabilized at a desirable (constant) set-point reference $r \in \mathbb{R}$. Motivated by the widespread use of PID-type controllers in industrial practice, we consider the design of PID-like control structures.

To make this more precise, we are considering an error-based feedback PID control action u_{PID} corresponding to

$$\begin{aligned} u_{\text{PID}} &:= -\bar{k}_p(s - r) - \bar{k}_i x_c - \bar{k}_d v, \\ \dot{x}_c &= s - r, \end{aligned} \quad (5)$$

where the controller state x_c is the integral of the position error $s - r$ and \bar{k}_p , \bar{k}_d , \bar{k}_i represent the proportional, derivative, and integral gains, respectively. We emphasize that the presence of an integrator action in controller (5) is motivated by the fact that it is able to compensate for an *unknown* static friction \bar{F}_s , which is typically the case in motion applications, so that the controller can robustly deal with the static friction effect.

By defining the overall state $z := (x_c, s - r, v)$, Equations (4) and (5) (with $u = u_{\text{PID}}$) can be written in a compact form as

$$\begin{aligned} \dot{z} &\in F_0(z) := A_0 z + b_0 \Psi(v), \\ A_0 &:= \begin{bmatrix} 0 & 1 & 0 \\ 0 & 0 & 1 \\ -\bar{k}_i & -\bar{k}_p & -\bar{k}_d \end{bmatrix}, \quad b_0 := \begin{bmatrix} 0 \\ 0 \\ 1 \end{bmatrix}, \end{aligned} \quad (6a)$$

where the nonlinear friction component Ψ is given by

$$\Psi(v) := -F_s \text{Sign}(v) + \psi(v), \quad (6b)$$

and we introduced the normalized parameters

$$k_p := \frac{\bar{k}_p}{m}, \quad k_d := \frac{\bar{k}_d + \bar{\alpha}_v}{m}, \quad k_i := \frac{\bar{k}_i}{m}, \quad F_s := \frac{\bar{F}_s}{m}, \quad \psi(v) := \frac{\bar{\psi}(v)}{m}. \quad (7)$$

We observe that matrix pair (A_0, b_0) naturally takes a controllable canonical form.

Remark 1. As emphasized in [51] and [22], the closed-loop dynamics described by (6) can be mathematically interpreted as the Filippov regularization [38] of any alternative discontinuous description of the nonsmooth friction phenomenon obtained by replacing (4) by the single valued right-hand side

$$\dot{v} = \begin{cases} \frac{1}{m}(-\bar{F}_s \text{sign}(v) - \bar{\alpha}_v v + \bar{\psi}(v) + u_{\text{PID}}), & \text{if } v \neq 0 \\ \text{“don’t care”}, & \text{if } v = 0, \end{cases} \quad (8)$$

where the “don’t care” selection does not make any difference in the Filippov regularization (which discards sets of measure zero such as the collection of states where $v = 0$). Since this regularization is well-posed according to [38], the existence of solutions is structurally guaranteed. One may be tempted to believe that this Filippov regularization introduces extra solutions as compared to (8), due to the “Filippov-enriched” right-hand side. Lemma 1 below clarifies that this is not the case because solutions are unique. \lrcorner

The following lemma, whose proof is a straightforward extension of [22, Lemma 1] (see also [18, Lemma 1]) establishes desirable properties of model (6).

Lemma 1. *If ψ is globally Lipschitz, then for any initial condition $z(0) \in \mathbb{R}^3$, system (6) has a unique solution² defined for all $t \geq 0$.*

Remark 2. Lemma 1 can also be proven by taking a different perspective based on maximal monotone operators, see [24, 57, 68]. In fact, system (6) can be written as $-\dot{z} \in \Gamma(z) + \gamma(z)$, where $\Gamma(z) = b_0 F_s \text{Sign}(b_0^\top z)$ defines a maximally monotone operator Γ and $\gamma(z) = -A_0 z - b_0 \psi(b_0^\top z)$ defines a globally Lipschitz function γ under the stated assumptions. In this case the celebrated work of Brezis [24] establishes the existence and uniqueness of a solution to (6) from any initial condition, see Theorem 3.17 together with Proposition 3.8 (as we are working in a finite-dimensional state space) and Remark 3.14 in [24]. \lrcorner

Given the popularity of PID controllers in the industry, we employ here reset enhancements that can be used in parallel with a classical PID scheme. In this way, no additional (complex) design and tuning procedures need to be performed, which lowers the threshold of using our proposed PID-based reset controllers in practice. Our control problem then corresponds to the following qualitative goal.

Problem 1. *For the plant in (4), design reset-enhanced PID controllers that*

²We consider a *solution* to (6) to be any locally absolutely continuous function \mathbf{z} that satisfies $\dot{\mathbf{z}}(t) \in F_0(\mathbf{z}(t))$ for almost all t in its domain.

1. globally asymptotically stabilize setpoint $(s, v) = (r, 0)$ for any constant r , robustly with respect to any unknown static friction F_s ;

2. result in short settling times (thereby providing good transient performance).

The design of reset enhancements for PID controllers differs significantly depending on whether the friction force is of Coulomb or Stribeck type. Hence, we describe more precisely these two scenarios in Section 2.3 below. The motivation for introducing reset enhancements is presented in Section 3.

2.3. The Coulomb and Stribeck scenarios

In this paper we will address two relevant scenarios for the closed-loop model (5), (4) (equivalently, (6)), characterized by the following two assumptions.

Assumption 1. (Coulomb friction) *The scaled velocity weakening component ψ in (6b) is identically zero.*³

Moreover, the normalized gains k_p , k_d and k_i in (7) satisfy $k_i > 0$, $k_p > 0$, $k_d k_p > k_i$, which is equivalent to the matrix A_0 in (6) being Hurwitz.

Assumption 2. (Stribeck friction) *The scaled velocity weakening component ψ in (6b) is globally Lipschitz and satisfies $|\psi(v)| \leq F_s$ and $v\psi(v) \geq 0$ for all v , and is linear in a small enough interval around zero (namely, for some ε_v , $|v| \leq \varepsilon_v \Rightarrow \psi(v) = L_2 v$).*⁴

Moreover, the normalized gains k_p , k_d and k_i in (7) satisfy $k_i > 0$, $k_p > 0$, $k_d k_p > k_i$, equivalently, matrix A_0 in (6) is Hurwitz.

We emphasize that Assumption 1 is stronger than (implies) Assumption 2, but characterizes a simplified setting addressed in [8] and more recently addressed in our works [22, 17]. Assumption 2 is weaker and therefore requires more advanced techniques, presented in [18]. These assumptions are exemplified in Figure 3.

Remark 3. Under the stated assumptions on ψ , it holds that $\Psi(v) \subseteq [-F_s, F_s]$ for all v , hence the PID-controlled system (6) evolves like a linear dynamical systems subject to a globally bounded input. Well-known results about bounded stabilization of linear systems [75] establish that global exponential stability of the origin of these systems can only be obtained if the underlying linear dynamics (that is, the one governed by A_0) is exponentially stable. This is the main motivation for the Hurwitz assumption on A_0 , namely there is no interest in addressing situations where the PID feedback is not stabilizing in the absence of Coulomb and Stribeck effects. \square

³Equivalently, the velocity weakening component $\bar{\psi}$ in (2) is identically zero.

⁴Equivalently, the velocity weakening component $\bar{\psi}$ in (2) is globally Lipschitz and satisfies $|\bar{\psi}(v)| \leq \bar{F}_s$ and $v\bar{\psi}(v) \geq 0$ for all v , and is linear in a small enough interval around zero (namely, for some $\bar{\varepsilon}_v$, $|v| \leq \bar{\varepsilon}_v \Rightarrow \bar{\psi}(v) = \bar{L}_2 v$).

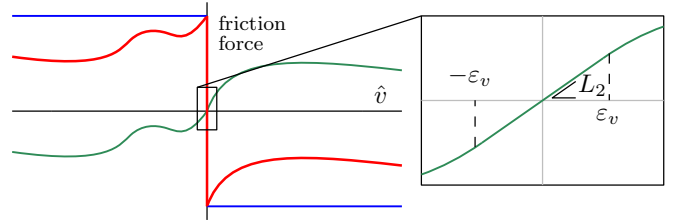


Figure 3: Nonlinear component Ψ of the friction graph satisfying Assumption 2. Overall effect Ψ (—), static contribution F_s (—), velocity-dependent contribution ψ (—). Assumption 1 corresponds to the green curve being zero (namely the red curve coincides with the blue one).

Under either Assumption 1 or 2, it is straightforward to prove that the set of all the equilibria of dynamics (6) is exactly the following compact set (appearing as a segment in the three-dimensional state space):

$$\mathcal{A} := \{z = (x_c, s - r, v) : s - r = v = 0, k_i x_c \in [-F_s, F_s]\}. \quad (9)$$

We emphasize that any element of \mathcal{A} is such that the position error $s - r$ and the velocity v are both zero and is therefore a desirable equilibrium from the point of view of Problem 1. On the other hand, the fact that a continuum of equilibria exist in \mathcal{A} makes the stabilization problem challenging and requiring non-standard concepts of set stability, generalizing the usual stability properties of isolated equilibria (e.g., the origin).

In the next section we will demonstrate the problems that arise with standard PID control in the two scenarios corresponding to Assumptions 1 and 2, thereby highlighting the challenges and the need for new control strategies. Then in the rest of the paper we will propose several advanced control strategies comprising extensions of PID controllers exploiting ideas from reset control. These extension will be shown to outperform the classical PID controllers described in (5).

3. Simulation and limitations of classical PID

The presence of a set-valued friction calls for dedicated numerical tools to simulate system (6) (or (6) with the reset enhancements presented in this paper). To this end, we provide in Section 3.1 a numerical scheme based on well-known time-stepping techniques, but specialized for (6). This allows us to illustrate in Section 3.2 the corresponding evolutions of (6) in the Coulomb and Stribeck scenarios, which already show the limitations of classical PID controllers and provide motivations for the proposed reset enhancements.

3.1. Simulation using time-stepping techniques

Even though Lemma 1 ensures that under Assumptions 1 and 2 dynamics (6) has unique solutions, simulating this unique solution from a specific initial condition is not a trivial task. Indeed, in the stick phase the correct value

of the friction force u_f cannot be determined only based on the velocity v . We discuss in this section a *time-stepping* simulation framework that can be effectively used to compute the solution by suitably determining the friction force at each simulated time instant. The time-stepping method is discussed here in a concise manner. More in-depth information can be found in, e.g., [50] and [2].

The equations of motion of the considered closed-loop system follows from (6) and are given by

$$\begin{aligned} m\dot{v} - h(v) - \bar{k}_p(s - r) - \bar{k}_d v - \bar{k}_i x_c &= \lambda, \\ \dot{x}_c &= s - r, \end{aligned} \quad (10)$$

with $h(v) := \bar{\psi}(v) + \bar{\alpha}_v v$ the smooth friction forces, and where λ denotes the Coulomb friction force which satisfies the set-valued force law

$$\lambda \in -\bar{F}_s \text{Sign}(v). \quad (11)$$

In order to suitably implement the constitutive friction force law in a time stepping algorithm, we express (11) in the form of an implicit *equation* (instead of an inclusion). To this end, we employ an equivalent formulation using the concept of a proximal point on a convex set. The proximal point y^* on a closed set C is defined as follows:

$$y^* = \text{prox}_C(y) := \text{argmin}_{y^* \in C} \|y - y^*\|, \quad (12)$$

which we use to equivalently write the set-valued force law (11) in proximal point formulation as follows:

$$\lambda = \text{prox}_C(\lambda - \mu v), \quad C = \{\lambda: -\bar{F}_s \leq \lambda \leq \bar{F}_s\}, \quad \mu > 0. \quad (13)$$

Note that the proximal point formulation in (13) is indeed equivalent to the set-valued friction law (11), which can be verified by evaluating all possible λ :

1. $|\lambda| > \bar{F}_s$: not possible, as λ lies outside the set C ;
2. $\lambda = \bar{F}_s$: we have $\bar{F}_s = \text{prox}_C(\bar{F}_s - \mu v)$, which yields $v \leq 0$ because $\mu > 0$, i.e., negative sliding or stick;
3. $-\bar{F}_s < \lambda < \bar{F}_s$: λ lies in the interior of C , i.e., stick;
4. $\lambda = -\bar{F}_s$: we have $-\bar{F}_s = \text{prox}_C(-\bar{F}_s - \mu v)$, which yields $v \geq 0$ because $\mu > 0$, i.e., positive sliding or stick.

We care to stress that the proximal point formulation of the set-valued Coulomb force law (13) is an *implicit* equation, which still expresses a set-valued force law. The actual friction force is determined, at every specific time instant, by both the force law and the equations of motion.

We will now discuss the well-known time-stepping algorithm of Moreau (see, e.g., [2, Chap. 10]). The method is based on a time discretization of the position s and velocity v using a fixed step size. Consider a single step of length Δt from starting time t_A to end time t_E , whereby $t_E = t_A + \Delta t$. The position s_A and velocity v_A are known

Algorithm 1 time-stepping using fixed-point iteration

```

1:  $s_A[0] = s_E[0] = s_0, v_A[0] = v_E[0] = v_0, x_c[0] = e_{i,0}$ ;
2: for  $k = 1, 2, \dots, N$  do
3:    $s_A[k] = s_E[k - 1]; v_A[k] = v_E[k - 1]$ ;
4:    $s_M[k] = s_A[k] + \frac{1}{2}\Delta t v_A[k]$ ;
5:    $x_c[k] = \frac{1}{2}\Delta t (s_A[k - 1] + s_A[k])$ ;
6:   converged = 0;  $i = 0; \tilde{\lambda}[0] = 0$ ;
7:   while not converged do
8:      $i = i + 1$ ;
9:      $\tilde{v}_E[i] = \frac{1}{m} \left( \bar{\psi}(v_A[k]) - \bar{k}_p(s_A[k] - r) - \bar{k}_d v_A[k] - \bar{k}_i x_c[k] + \tilde{\lambda}[i - 1] \right) \Delta t + v_A[k]$ ;
10:     $\tilde{\lambda}[i] = \min \left( \max \left( -\bar{F}_s, \tilde{\lambda}[i - 1] - \mu \tilde{v}_E[i] \right), \bar{F}_s \right)$ ;
11:    error =  $|\tilde{\lambda}[i] - \tilde{\lambda}[i - 1]|$ ;
12:    converged if: error < tolerance;
13:   end while
14:    $\lambda[k] = \tilde{\lambda}[i]; v_E[k] = \tilde{v}_E[i]$ ;
15:    $s_E[k] = s_M[k] + \frac{1}{2}\Delta t v_E[k]$ ;
16: end for

```

at $t = t_A$. First, the algorithm performs a mid-step⁵: $s_M = s_A + \frac{1}{2}\Delta t v_A$. Now, discretizing the equation of motion (10) yields

$$\begin{aligned} m(v_E - v_A) &= h(v_A)\Delta t - \bar{k}_p(s_A - r)\Delta t \\ &\quad - \bar{k}_d v_A \Delta t - \bar{k}_i x_c \Delta t + \lambda \Delta t, \end{aligned} \quad (14)$$

where v_E and λ are unknown. The controller state x_c can be determined by a numerical integration scheme (e.g., backward Euler or midpoint rule), as we show later on. The set of equations to be solved by the time-stepping routine is given by (13) and (14). This set of nonlinear algebraic equations must be solved to obtain the unknowns v_E and λ , which can be done by several numerical techniques such as Newton's method or fixed-point iteration. To this end, the prox-function in (13) can be easily implemented by rewriting the function as a "min-max" function, i.e., $\text{prox}_C(y) = \min(\max(-\bar{F}_s, y), \bar{F}_s)$, for C as in (13). Note that this function corresponds to saturating variable y between the values $-\bar{F}_s$ and \bar{F}_s . When the velocity and friction force at the end of the time step are obtained, the procedure is completed by calculating the position at $t = t_E$: $s_E = s_M + \frac{1}{2}\Delta t v_E$.

We provide a pseudo-code example in Algorithm 1 that can be used to simulate the controlled frictional system. The initial conditions $s(0) = s_0$, $v(0) = v_0$, and $x_c(0) = x_{c,0}$ are assumed to be known, and a fixed-point iteration scheme is used to determine the velocity and friction force at the end of each time step. Note that we use the auxiliary variables $\tilde{\lambda}$ and \tilde{v}_E (with index i) within the iteration loop to iteratively solve (13),(14). The parameter μ in (13) is

⁵In a more general setting, the midpoint is often used to determine whether or not the contact is closed, which is always the case in our situation.

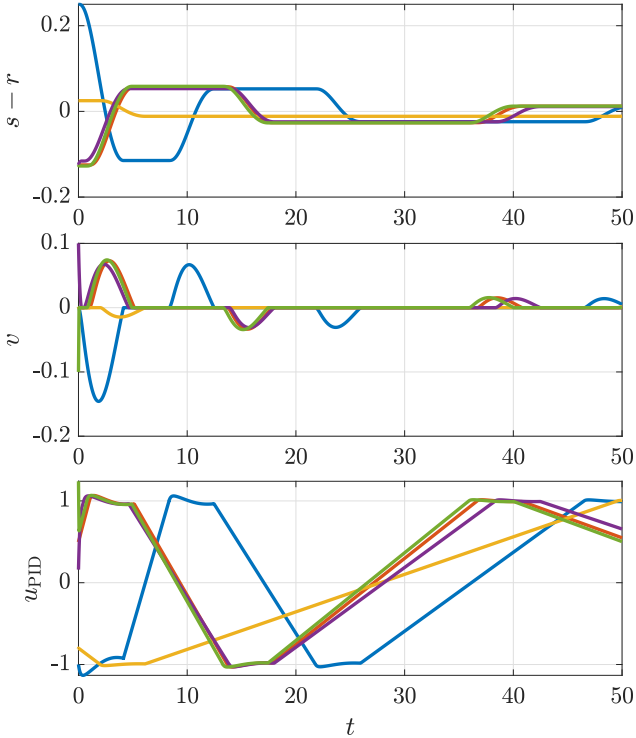


Figure 4: Simulations with the parameters of Table 1 and Coulomb friction (namely $\psi \equiv 0$) and without reset compensation. Evolutions of $s - r$ (top), v (middle) and u_{PID} (bottom). Slow convergence is apparent from the top plot.

a tuning parameter trading off convergence speed versus accuracy, and “tolerance” is a user-defined error criterion of the fixed-point iteration. Finally, we use a trapezoidal numerical scheme to determine the integral action of the PID controller at each time step, without loss of generality.

Remark 4. Above we discussed the time-stepping scheme that we apply throughout this paper for simulating systems with friction. Strictly speaking, the algorithm is more complicated than needed as it also applies to systems with impacts (in case, for instance, of unilateral constraints in mechanical systems), see, e.g., [2]. Indeed, we could also have used the more basic backward Euler scheme of the form $\frac{z_{k+1} - z_k}{h} \in A_0 z_{k+1} + b_0 \psi(b_0^\top z_{k+1}) - b_0 F_s \text{Sign}(b_0^\top z_{k+1})$, where h is the fixed step size. This scheme stems originally from the work of Moreau [58], where it was used for approximating the evolution of dynamical systems called sweeping processes $-\dot{x} \in \partial\varphi(t, x)$, where $\partial\varphi$ denotes the subdifferential of a convex function φ , see, e.g., [24, 57, 68]. In fact, note that our set-valued Coulomb friction characteristic $v \mapsto \text{Sign}(v)$ is the subdifferential of the absolute value function $v \mapsto |v|$, and $\Gamma : z \mapsto b_0 F_s \text{Sign}(b_0^\top z)$ can be written as the subdifferential of the convex function $z \mapsto F_s |b_0^\top z|$. Note that subdifferentials of (lower semi-continuous) convex functions are maximally monotone, see Remark 2. The consistency (in the sense that the numerical approximations converge to an actual solution of the differential inclusion when the step size h goes

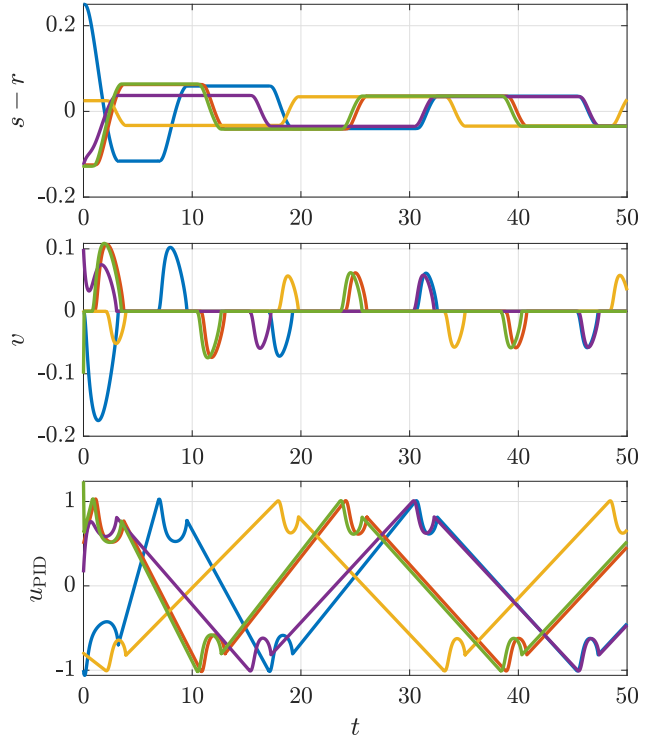


Figure 5: Simulations with the parameters of Table 1 and Stribeck friction (namely ψ as in (15)) and without reset compensation. Evolutions of $s - r$ (top), v (middle) and u_{PID} (bottom). Persistent oscillations are apparent from the top plot.

to zero) of Moreau’s backward Euler scheme (under maximal monotonicity assumptions) has been studied extensively, see, e.g. [68, 58, 25] and the references therein. For the consistency of backward-Euler-based schemes for the computation of periodic solutions to maximally monotone differential inclusions, see, e.g., [45]. \lrcorner

Remark 5. The time-stepping scheme of Algorithm 1 can be extended to cope with reset control strategies. In such a case, the reset conditions should be evaluated at the beginning of each time-step, and adapt the integrator state e_i in accordance with the reset map before entering the “while”-loop. The time stepping framework is then essentially combined with an event-driven scheme. \lrcorner

3.2. Limitations of classical PID control

With Algorithm 1 we can simulate (6) for the two scenarios of Coulomb and Stribeck friction characterized in Assumptions 1 and 2. For the Coulomb case we select $\psi \equiv 0$ in (6b), whereas for the Stribeck case we select

$$\psi(v) = \begin{cases} L_2 v, & |v| \leq \varepsilon_v \\ (F_s - F_\infty) \kappa v / (1 + \kappa |v|), & |v| > \varepsilon_v. \end{cases} \quad (15)$$

with $F_\infty \leq F_s$. In particular, we use the parameters reported in Table 1, providing the function ψ represented in Figure 6. This selection clearly satisfies Assumption 2.

Parameter and corresponding symbol		Value
Static friction	F_s	1
Velocity weakening zero-velocity slope	L_2	12.8
Velocity weakening linear half-interval	ε_v	10^{-3}
Velocity weakening asymptotic term	F_∞	1/3
Velocity weakening shape parameter	κ	20
Proportional gain	k_p	3
Integral gain	k_i	4
Derivative gain	k_d	6.4
Coulomb reset compensation factor	α	1
Mass	m	1
Viscous friction	$\bar{\alpha}_v$	0

Table 1: Parameters considered for the simulations of the paper.

The PID gains in Table 1 are selected in such a way that matrix A_0 in (6) has two dominant complex conjugate eigenvalues and a real one (namely, $-0.19 \pm i0.79$ and -6.01). This configuration corresponds to the PID tuning (on the linear part through loop-shaping) achieving fast response times at the cost of some overshoot. This choice is most typical to obtain fast positioning in high-precision motion systems and is therefore the main setting discussed throughout this paper. Nevertheless, in our Assumptions 1 and 2 we only enforce a mild requirement that A_0 be Hurwitz and this leads to two other characteristic configurations: the case where A_0 has all real eigenvalues or has a dominant real eigenvalue and two complex conjugate ones. These two alternative settings are less interesting technologically and are briefly illustrated in Section 8.

Solutions to (6) for different initial conditions (each initial condition corresponding to a color) in the two scenarios of Coulomb and Stribeck friction are reported, respectively, in Figures 4 and 5. In the figures, the control input u_{PID} is obtained from (5) and (7) with the values of m and $\bar{\alpha}_v$ reported in Table 1.

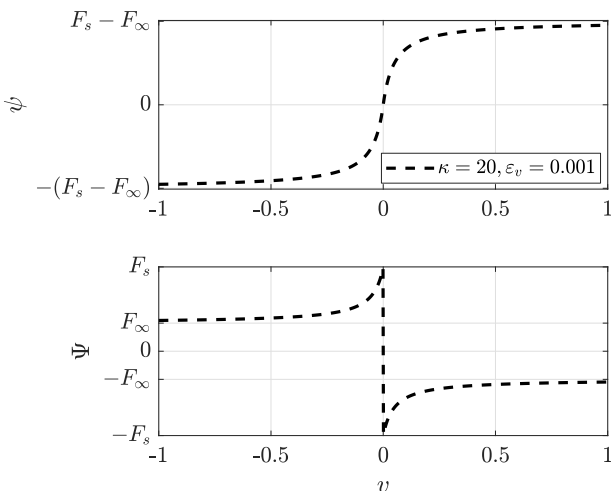


Figure 6: Function ψ given in (15) and with the parameters given in Table 1, and corresponding graph of Ψ in (6b).

The simulation in Figure 4 (Coulomb scenario) illustrates that a classical PID controller induces asymptotic convergence to the setpoint $(s, v) = (r, 0)$, but also that the presence of Coulomb friction induces long stick phases when $s - r$ is constant and u_{PID} evolves according to linear ramps in time (due to the dynamics $\dot{x}_c = s - r$ for the integral error). The depleting and refilling of the integral error associated with these ramps can be avoided through a reset action on x_c when entering a stick phase, as detailed in Section 5, and motivate reset enhancements of PID controllers to improve settling times.

The simulation in Figure 5 (Stribeck scenario) illustrates that a classical PID controller does *not* provide solutions converging to the setpoint $(s, v) = (r, 0)$, due to the persistent periodic oscillations of $s - r$ (the so-called hunting phenomenon). This limitation of a classical PID controller can also be overcome by reset enhancements, as detailed in Section 6.

4. A Lyapunov perspective on the stability of \mathcal{A}

4.1. Stick and slip observed from insightful coordinates

The simulations of Figures 4 and 5 clearly reveal the stick-slip nature of the solutions to (6). To better understand and characterize this behavior, it is convenient to represent dynamics (6) via the next coordinate transformation, proposed in [22],

$$x := \begin{bmatrix} \sigma \\ \phi \\ v \end{bmatrix} := \begin{bmatrix} -k_i(s-r) \\ -k_p(s-r) - k_i x_c \\ v \end{bmatrix}, \quad (16)$$

where σ is a generalized position error, ϕ is the controller state encompassing the proportional and integral control actions, and v is the velocity of the mass.

This change of coordinates is nonsingular under Assumption 1 or 2 (k_i and k_p are positive) and it rewrites (6) as

$$\dot{x} \in F(x) := Ax + b_0 \Psi(v), \quad (17)$$

$$A := \begin{bmatrix} 0 & 0 & -k_i \\ 1 & 0 & -k_p \\ 0 & 1 & -k_d \end{bmatrix}, \quad b_0 := \begin{bmatrix} 0 \\ 0 \\ 1 \end{bmatrix}$$

with the set-valued map Ψ defined in (6b). As compared to (6), here matrix A takes an observable canonical form.

A first reason for introducing the new representation (17) is that the set of equilibria \mathcal{A} in (9) simplifies to

$$\mathcal{A} = \{x \in \mathbb{R}^3 : \sigma = v = 0, |\phi| \leq F_s\}, \quad (18)$$

which, unlike (9), is independent of the PID gains. The simple expression of \mathcal{A} in (18) allows writing explicitly the Euclidean distance of a point x to \mathcal{A} as

$$|x|_{\mathcal{A}}^2 := \left(\inf_{y \in \mathcal{A}} |x - y| \right)^2 = \sigma^2 + v^2 + dz_{F_s}(\phi)^2 \quad (19)$$

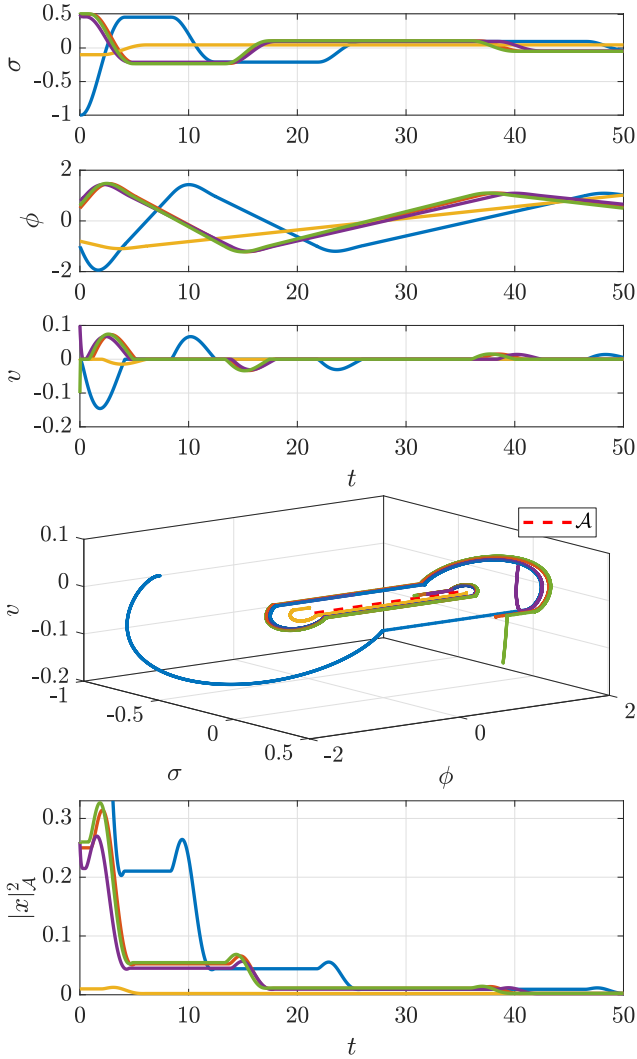


Figure 7: Solutions of Figure 4 (Coulomb friction) represented in the coordinates (16) and the corresponding distance from \mathcal{A} in (19).

where $\text{dz}_{F_s}(\phi) := \phi - F_s \text{sat}(\phi/F_s)$ is the symmetric scalar deadzone function returning zero when $\phi \in [-F_s, F_s]$. Indeed, the rightmost expression in (19) follows from separating the cases $\phi < -F_s$, $|\phi| \leq F_s$, $\phi > F_s$ and applying the definition given by the middle expression of (19).

A second reason for using coordinates x in (16) is that these provide a simplified representation of the sets where solutions are in the stick phase (the intervals where the top plots of Figures 4 and 5 are flat, namely the intervals where $v \equiv 0$) or in the slip phase (the time intervals associated to the speed bumps in the middle plots of Figures 4 and 5). In particular, we may define

$$\mathcal{E}_{\text{stick}} := \{x \in \mathbb{R}^3 : v = 0, |\phi| \leq F_s\}, \quad (20a)$$

$$\mathcal{E}_{\text{slip}} := \mathbb{R}^3 \setminus \mathcal{E}_{\text{stick}}. \quad (20b)$$

More specifically, the generalized controller state ϕ represents all the nonzero components of the control action at zero velocity (that is, the proportional and integral terms), and according to (20), the size of ϕ compared to

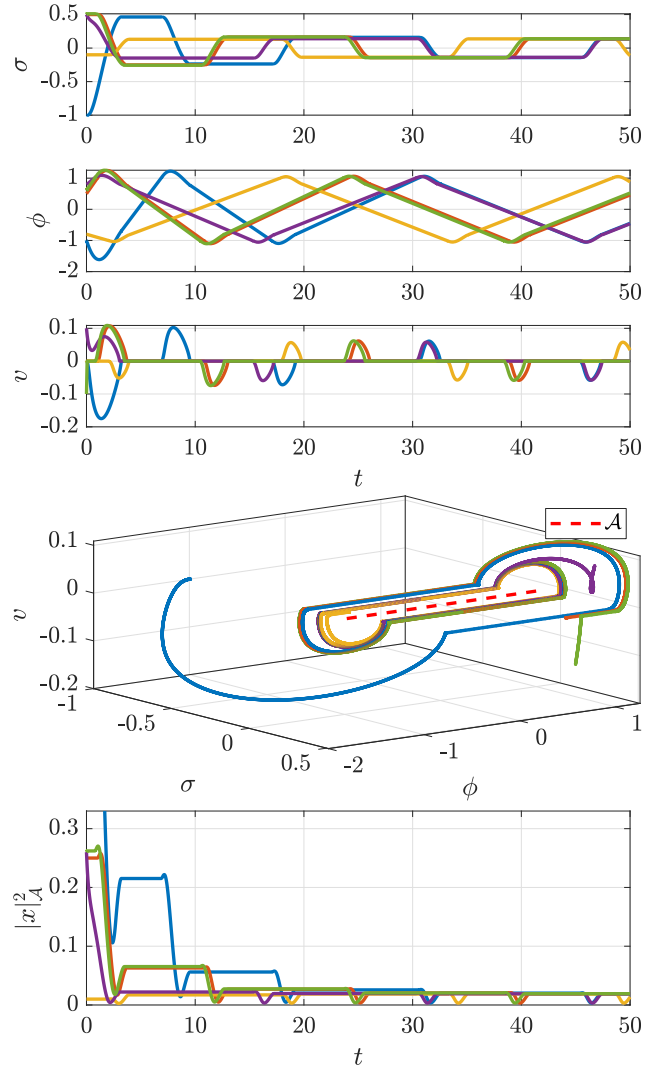


Figure 8: Solutions of Figure 5 (Stribeck friction) represented in the coordinates (16) and the corresponding distance from \mathcal{A} in (19).

the static friction F_s at $v = 0$ determines whether the solution evolves in a stick phase or not.

The same simulations reported in Figures 4 and 5 (corresponding to the parameters selection in Table 1) are represented in Figures 7 and 8 using the new coordinates $x = (\sigma, \phi, v)$ of (16), shown in the three top plots. The 3D plots in the middle of Figures 7 and 8 show the corresponding phase portraits and provide an insightful interpretation of the evolution of the solutions with respect to the attractor \mathcal{A} in (18), which is represented as a dashed red segment.

In both figures, solutions revolve around the attractor through alternating slip phases (in the two tilted regions $\mathcal{E}_{\text{slip}}$ where $|\phi| > F_s$) and stick phases (in the flat region $\mathcal{E}_{\text{stick}}$ where $v = 0$ and $|\phi| < F_s$). Moreover, from Figure 7 we observe that in the Coulomb case solutions slowly approach the attractor (the slow convergence phenomenon) while in the Stribeck case, these solutions settle on a persistent oscillation away from the attractor (the hunting

phenomenon). This fact is confirmed by the bottom plots of Figures 7 and 8, showing the evolution of the (squared) distance to \mathcal{A} defined in (19). In summary, Figures 4 and 5 clearly illustrate the fact that $|x|_{\mathcal{A}}$ converges to zero in the Coulomb case and exhibits persistent oscillations (instability) in the Stribeck case.

The simulations reported in Figure 7 suggest that, under Assumption 1, the PID controlled feedback is globally asymptotically stable. This statement is the main result of [22] and is stated below.

Theorem 1. *Under Assumption 1, the compact set \mathcal{A} in (9) is globally \mathcal{KL} asymptotically stable for (6). Equivalently, the compact set in (18) is globally \mathcal{KL} asymptotically stable for (17). Namely, there exists a class \mathcal{KL} function β such that all solutions x satisfy*

$$|x(t)|_{\mathcal{A}} \leq \beta(|x(0)|_{\mathcal{A}}, t), \quad \forall t \geq 0, \quad (21)$$

where the distance $|x|_{\mathcal{A}}$ of x from \mathcal{A} is defined in (19).

Note that no smaller set could be proven to be globally attractive (therefore asymptotically stable) because \mathcal{A} is a union of equilibria. It is also emphasized in [22] that the stated stability property is robust to perturbations as an immediate consequence of the results in [41, Ch. 7] and the well-posedness of dynamics (6) (equivalently, (17)).

Remark 6. Theorem 1 addresses the case of a symmetric Coulomb friction $F_s \text{Sign}(v)$ in (6b) (with $\psi(v) \equiv 0$, but it easily extends to the case of a translated attractor, when considering *asymmetric* Coulomb friction $F_s \text{Sign}(v) - \psi_0$, for any constant scalar $\psi_0 \in \mathbb{R}$. This fact can be proven by shifting by ψ_0 the coordinate ϕ introduced in Section 4.1 and observing that the closed-loop description (17) remains the same and is independent of ψ_0 . \lrcorner

In Sections 4.2 and 4.3, the analysis of key system properties and a Lyapunov function are presented that underlie the technical proof of Theorem 1, but also form a stepping stone towards the analysis and design of reset controllers in later sections.

4.2. Semiglobal dwell time and hybrid extended model

Representation (17) provides a clear understanding of the main effect of the set-valued nature of Coulomb friction (the vertical line at $v = 0$ in Figure 3), which literally tears apart the two half-spaces where $\phi > F_s$ and $\phi < -F_s$ by introducing a “stick band” surrounding the line $v = 0, \phi = 0$ and corresponding to set $\mathcal{E}_{\text{stick}}$ in (20a) and to the flat surface in the 3D plots of Figures 7-8. Without static friction (namely when $F_s = 0$), the two half-spaces reconnect and the dynamics reduces to a PID-controlled mass with a single-valued friction element that is linear in the Coulomb case and nonlinear in the Stribeck case.

Although the effect of Coulomb friction is elegantly and concisely represented by the differential inclusion model in

(17), one may equivalently represent the solutions simulated in Figures 7-8 as nonsmoothly transitioning between two types of dynamical evolutions associated with the stick and slip phases. The advantage of such an alternative description is that it allows building a hybrid extended model whose transition from stick to slip (and viceversa) is conveniently represented by discrete jumps of an additional logical variable, and whose stability properties are easier to certify by means of hybrid Lyapunov functions. This approach is exploited here for the Coulomb case of Assumption 1 and in Section 6 for the Stribeck case of Assumption 2.

To suitably define a hybrid extended model, consider first the following sets intuitively associated with a stick-to-slip transition:

$$\begin{aligned} S_1 &:= \{x: v = 0 \wedge (\phi > F_s \vee (\phi = F_s \wedge \sigma > 0))\} \\ S_{-1} &:= \{x: v = 0 \wedge (\phi < -F_s \vee (\phi = -F_s \wedge \sigma < 0))\}. \end{aligned} \quad (22)$$

Then the following *semi-global dwell-time* result has been proven in [21, Lemma 1] for the Coulomb case of Assumption 1.

Lemma 2. *Under Assumption 1, for each compact set \mathcal{K} , there exists $\delta(\mathcal{K}) > 0$ such that each solution $x = (\sigma, \phi, v)$ of (17) starting in \mathcal{K} satisfies the following. For any t such that $x(t) \in S_1 \cup S_{-1}$, it holds that*

$$\begin{aligned} x(t) \in S_1 &\implies v(s) \geq 0, \\ x(t) \in S_{-1} &\implies v(s) \leq 0, \end{aligned}$$

for all $s \in [t, t + \delta(\mathcal{K})]$.

Intuitively speaking, Lemma 2 states that once a solution performs a stick-to-slip transition, it cannot perform a subsequent stick-to-slip transition unless a minimum positive time (namely, at least $\delta(\mathcal{K})$ time units) has elapsed. Note that for any compact set \mathcal{K} of initial conditions, the quantity $\delta(\mathcal{K})$ remains uniform over all solutions starting from that specific compact set. Of course $\delta(\mathcal{K})$ is expected to shrink to zero as \mathcal{K} becomes increasingly larger, because increasingly large speeds are accounted for in the corresponding solutions.

Remark 7. A key property needed for proving the uniformity stated in Lemma 2 is that for any compact set \mathcal{K} , the ensuing solutions are uniformly bounded. This boundedness result easily follows from the fact that, under Assumption 1, the set-valued map Ψ is uniformly bounded by F_s and acts, in (17), on an exponentially stable linear system, which is then clearly BIBO stable. \lrcorner

As suggested in [21], based on Lemma 2, we may introduce the following hybrid extended model capable of semiglobally *representing* dynamics (17). More precisely, the next model semiglobally reproduces the solutions of (17) in the sense rigorously characterized in Lemma 3 below. The extended hybrid model enables constructing

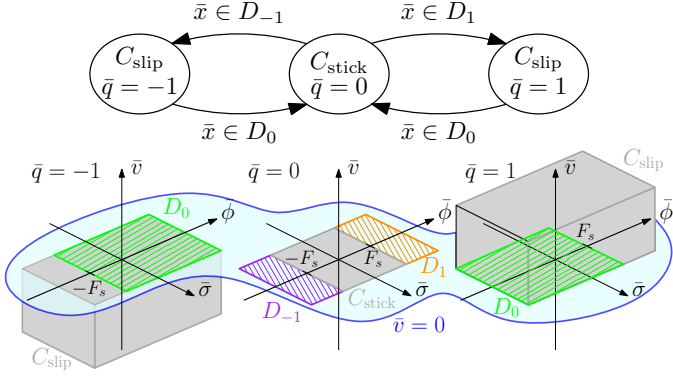


Figure 9: Top: hybrid automaton underlying (23). Bottom: “projections” to the $(\bar{\sigma}, \bar{\phi}, \bar{v})$ space of the flow and jump sets in (23f)-(23j).

simplified Lyapunov functions to prove Theorem 1 and is parametrized by quantity δ from Lemma 2. Its extended state augments the state x in (17) with a logical variable \bar{q} and a timer $\bar{\tau}$, and corresponds to

$$\bar{x} := (\bar{\sigma}, \bar{\phi}, \bar{v}, \bar{q}, \bar{\tau}) \in \bar{\Xi} := \mathbb{R}^3 \times \{-1, 0, 1\} \times [0, 2\delta], \quad (23a)$$

where $\bar{q} \in \{-1, 0, 1\}$ characterizes positive ($\bar{q} = 1$) or negative ($\bar{q} = -1$) velocity slip, or stick ($\bar{q} = 0$). Variable $\bar{\tau}$ prevents unwanted artificial Zeno solutions. The hybrid extended model \mathcal{H}_δ is defined as follows, using the framework in [41],

$$\mathcal{H}_\delta : \begin{cases} \dot{\bar{x}} = \bar{f}(\bar{x}), & \bar{x} \in \bar{C} := C_{\text{slip}} \cup C_{\text{stick}} \\ \bar{x}^+ \in \bar{G}(\bar{x}), & \bar{x} \in \bar{D} := \bigcup_{i \in \{1, -1, 0\}} D_i, \end{cases} \quad (23b) \quad (23c)$$

where the flow and jump maps are given by

$$\bar{f}(\bar{x}) := \begin{bmatrix} -k_i \bar{v} \\ \bar{\sigma} - k_p \bar{v} \\ -k_d \bar{v} + |\bar{q}| \bar{\phi} - \bar{q} F_s \\ 0 \\ 1 - \text{dz}_1(\bar{\tau}/\delta) \end{bmatrix}, \quad \bar{G}(\bar{x}) := \bigcup_{i: \bar{x} \in D_i} \{g_i(\bar{x})\}, \quad (23d)$$

the different jump maps g_i are given by

$$g_1(\bar{x}) := \begin{bmatrix} \bar{\sigma} \\ \bar{\phi} \\ \bar{v} \\ 1 \\ 0 \end{bmatrix}, \quad g_{-1}(\bar{x}) := \begin{bmatrix} \bar{\sigma} \\ \bar{\phi} \\ \bar{v} \\ -1 \\ 0 \end{bmatrix}, \quad g_0(\bar{x}) := \begin{bmatrix} \bar{\sigma} \\ \bar{\phi} \\ \bar{v} \\ 0 \\ \bar{\tau} \end{bmatrix} \quad (23e)$$

and the flow and jump sets are given by

$$C_{\text{slip}} := \{\bar{x} \in \bar{\Xi} : |\bar{q}| = 1, \bar{q}\bar{v} \geq 0\} \quad (23f)$$

$$C_{\text{stick}} := \{\bar{x} \in \bar{\Xi} : \bar{q} = 0, \bar{v} = 0, |\bar{\phi}| \leq F_s\} \quad (23g)$$

$$D_1 := \{\bar{x} \in \bar{\Xi} : \bar{q} = 0, \bar{v} = 0, \bar{\phi} \geq F_s, \bar{\tau} \in [\delta, 2\delta]\} \quad (23h)$$

$$D_{-1} := \{\bar{x} \in \bar{\Xi} : \bar{q} = 0, \bar{v} = 0, \bar{\phi} \leq -F_s, \bar{\tau} \in [\delta, 2\delta]\} \quad (23i)$$

$$D_0 := \{\bar{x} \in \bar{\Xi} : |\bar{q}| = 1, \bar{v} = 0, \bar{q}\bar{\phi} \leq F_s\}. \quad (23j)$$

The flow and jump maps for $\bar{\tau}$ ensure the invariance of the set $[0, 2\delta]$ for $\bar{\tau}$, as per (23a). Since $D_i \cap D_k = \emptyset$ for $i, k \in \{-1, 0, 1\}$ and $i \neq k$, \bar{G} is actually always a *single-valued* mapping. A pictorial representation of (23) can be

found in Figure 9, which gives a clear hybrid automaton interpretation of (23) similar to the one discussed in [41, §1.4.2].

As an important observation, the first three components of the flow map in (23d) coincide in C_{slip} and C_{stick} with the right-hand sides of (17). Then, it is intuitive that a solution to \mathcal{H}_δ captures the solution to (17) when the condition $\bar{\tau} \in [\delta, 2\delta]$ is removed from (23h)-(23i). In such a case, however, (23) would also exhibit an undesired behavior associated to nonconverging Zeno solutions, not physically relevant, that keep jumping forever without ever flowing (e.g., one such defective solution would originate from the initial condition $\bar{v} = 0, \bar{\phi} = F_s, \bar{\sigma} \neq 0$). The timer $\bar{\tau}$ in \mathcal{H}_δ removes these Zeno solutions, and exploits the inherent dwell-time property of solutions to (17) established in Lemma 2 to make sure that the (unique, from Lemma 1) solution to (17) is semiglobally captured by \mathcal{H}_δ . Indeed, after solutions to \mathcal{H}_δ exit a stick phase and enter a slip phase jumping from D_1 or D_{-1} , the timer is reset to zero via g_1 or g_{-1} and enforces that a time δ elapses before solutions exit a stick phase again (due to the condition $\bar{\tau} \in [\delta, 2\delta]$), which corresponds to the property of solutions to (17) in Lemma 2.

The fact that model \mathcal{H}_δ correctly represents, in a semiglobal fashion, dynamics (17) is established in the next lemma, which is proven in [21, Lemma 2].

Lemma 3. *Under Assumption 1, for each compact set $\mathcal{K} \subset \mathbb{R}^3$, there exists $\delta > 0$ satisfying the following. For each solution $t \mapsto x(t) = (\sigma(t), \phi(t), v(t))$ of (17) starting at $x_0 = (\sigma_0, \phi_0, v_0) \in \mathcal{K}$, there exist τ_0 and q_0 and a solution $\bar{x} = (\bar{\sigma}, \bar{\phi}, \bar{v}, \bar{\tau}, \bar{q})$ of \mathcal{H}_δ in (23) starting at $\bar{x}_0 = (\sigma_0, \phi_0, v_0, \tau_0, q_0)$ such that, for all $t \geq 0$,*

$$\bar{\sigma}(t, j(t)) = \sigma(t), \bar{\phi}(t, j(t)) = \phi(t), \bar{v}(t, j(t)) = v(t), \quad (24)$$

where $j(t) = \min_{j \in \mathbb{Z}} \{j : (t, j) \in \text{dom } \bar{x}\}$.

The intuition behind Lemma 3 is that there exists one solution to (23) that can evolve hybridly (by jumping and flowing) so as to reproduce the flowing solution to (17), although there might be other solutions to \mathcal{H}_δ that are not complete. An appealing feature of the hybrid automaton (23) is that the component \bar{q} of its solutions is informative about whether the solution is currently in a *stick phase* (then its physical components are evolving in $\mathcal{E}_{\text{stick}}$ as per (20)), in which case $\bar{q} = 0$, or in a *slip phase* with positive velocity ($\bar{q} = 1$) or negative velocity ($\bar{q} = -1$).

Remark 8. The above result demonstrates that on compact sets of initial states the hybrid model can reproduce the solutions of our differential inclusion model. An interesting connection on this result lies in the notion of (bi)simulation as used in computer science. In computer science, the notions of simulation (or bisimulation) relations have been used for approximations of purely discrete systems, see [30, 56], and, in recent years were also extended to continuous and hybrid systems [43, 66, 69, 83].

In fact, in these terms, one could say that the hybrid model (23) semi-globally “simulates” the differential inclusion (17), or, in other words, is a semi-global simulation model of the differential inclusion. This provides an interesting perspective on the statement in Lemma 3. \square

4.3. Lyapunov functions for proving Theorem 1

The proof of Theorem 1 given in [22] is quite technical and makes use of the *discontinuous* Lyapunov-like function

$$\begin{aligned} V(x) &:= \begin{bmatrix} \sigma \\ v \end{bmatrix}^\top \begin{bmatrix} \frac{k_d}{k_i} & -1 \\ -1 & k_p \end{bmatrix} \begin{bmatrix} \sigma \\ v \end{bmatrix} + \min_{\mathfrak{f} \in F_s \text{ Sign}(v)} |\phi - \mathfrak{f}|^2 \\ &= \min_{\mathfrak{f} \in F_s \text{ Sign}(v)} \begin{bmatrix} \sigma \\ \phi - \mathfrak{f} \end{bmatrix}^\top P \begin{bmatrix} \sigma \\ \phi - \mathfrak{f} \end{bmatrix}, \end{aligned} \quad (25a)$$

where the matrix P is given by

$$P := \begin{bmatrix} \frac{k_d}{k_i} & 0 & -1 \\ 0 & 1 & 0 \\ -1 & 0 & k_p \end{bmatrix}. \quad (25b)$$

Function (25a) is rather intuitive because P in (25b) is a positive definite solution to $A^\top P + PA \leq 0$ for A defined in (17) and V corresponds to the minimum quadratic form induced by P when accounting for all possible values allowed by the set-valued friction model. Note that for $v \neq 0$ the minimization in (25a) becomes trivial because \mathfrak{f} can take only the value $F_s \text{ sign}(v)$. Intuitively speaking, the second term in (25a) mimics the deadzone-shaped tearing visible in the 3D plot of Figure 7 and suitably accounts for the flat *stick* region associated with $v = 0$ and $|\phi| \leq F_s$.

Note that function V is discontinuous. For example, if we evaluate V along the sequence of points $(\sigma_k, \phi_k, v_k) = (0, 0, \varepsilon_k)$ for $\varepsilon_k \in (0, 1)$ converging to zero, V converges to F_s^2 , even though its value at zero is zero. Nevertheless, V is non-increasing along solutions and positive definite, as established in the next proposition, combining the results of [22, Lemma 2] and [18, Eq. (28)].

Proposition 1. *The Lyapunov-like function in (25) is lower semicontinuous and, under Assumption 1, it enjoys the following properties:*

1. $V(x) = 0$ for all $x \in \mathcal{A}$ and there exist $c_1 > 0$, $c_2 > 0$ such that, for all $x \in \mathbb{R}^3$,

$$c_1 |x|_{\mathcal{A}}^2 \leq V(x) \leq c_2 |x|_{\mathcal{A}}^2 + 2F_s^2$$

2. each solution $x = (\sigma, \phi, v)$ to (17) satisfies for all $t_2 \geq t_1 \geq 0$

$$V(x(t_2)) - V(x(t_1)) \leq -c \int_{t_1}^{t_2} v(t)^2 dt, \quad (26)$$

$$\text{with } c := 2(k_p k_d - k_i) > 0.$$

Besides its intuitive relevance, function V is only a first step towards the proof of Theorem 1 given in [22], which requires nontrivial tools from nonsmooth analysis. This

was a main motivation for introducing the hybrid extended model (23). Indeed, model (23) simplifies the Lyapunov characterization of the desirable behavior of solutions by way of introducing, in [21], an equivalent smooth version of function V , corresponding to

$$\begin{aligned} \bar{V}(\bar{x}) &:= \begin{bmatrix} \bar{\sigma} \\ \bar{v} \end{bmatrix}^\top \begin{bmatrix} \frac{k_d}{k_i} & -1 \\ -1 & k_p \end{bmatrix} \begin{bmatrix} \bar{\sigma} \\ \bar{v} \end{bmatrix} \\ &\quad + |\bar{q}|(\bar{\phi} - \bar{q}F_s)^2 + (1 - |\bar{q}|)(dz_{F_s}(\bar{\phi}))^2. \end{aligned} \quad (27)$$

Function \bar{V} is smooth in the extended state variable $\bar{x} := (\bar{\sigma}, \bar{\phi}, \bar{v}, \bar{q}, \bar{\tau})$ and it is natural to consider the extended counterpart of the attractor \mathcal{A} in (18) as

$$\bar{\mathcal{A}} := \{\bar{x} : \bar{\sigma} = \bar{v} = 0, \bar{\phi} \in F_s \text{ Sign}(\bar{q})\}.$$

With respect to this extended attractor, \bar{V} enjoys the properties in the next proposition (established in [21, Lemma 3]), where we emphasize that we may now use a (simpler) standard gradient in place of integral expression in (26).

Proposition 2. *Under Assumption 1, the Lyapunov function \bar{V} in (27) is*

- (i) *positive definite with respect to $\bar{\mathcal{A}}$ in $\bar{C} \cup \bar{D}$ and radially unbounded relative to $\bar{C} \cup \bar{D}$;*
- (ii) *with $c := 2(k_p k_d - k_i) > 0$ as in Proposition 1, the directional derivative of \bar{V} along the flow dynamics (23) satisfies*

$$\langle \nabla \bar{V}(\bar{x}), \bar{f}(\bar{x}) \rangle = -c\bar{v}^2, \quad \forall \bar{x} \in C_{\text{slip}} \cup C_{\text{stick}} \quad (28a)$$

- (iii) *for each $p \in \{1, -1, 0\}$, the jump dynamics of (23) satisfies*

$$\bar{V}(g) - \bar{V}(\bar{x}) \leq 0, \quad \forall \bar{x} \in \bar{D}, \forall g \in \bar{G}(\bar{x}). \quad (28b)$$

The matching and decreasing properties of V in Proposition 1 and of \bar{V} in Proposition 2 along their respective solutions are illustrated in Figure 10, where the same colors are used for solutions starting from the same initial conditions. As established in Lemma 3, the two functions provide matching evolutions in the t direction, even though it should be kept in mind that \bar{V} is evaluated along a hybrid solution of (23), whereas V is evaluated along a continuous-time solution of (17), (6b). At the bottom of Figure 10 we also represent the state variable \bar{q} , showing the different stick ($\bar{q} = 0$) and slip ($|\bar{q}| = 1$) phases of the corresponding hybrid solutions.

The advantage of using function \bar{V} for (23) over using function V for (17) comes from the fact that (28) enables applying in a straightforward way the hybrid invariance principle of [41, Ch. 8] to conclude global convergence to \mathcal{A} , whereas the global convergence proof of [22] (relying on V) required using an ad-hoc nonsmooth (and lengthy) proof. Providing simplified Lyapunov certificates of convergence (and stability) is key for moving on to the next

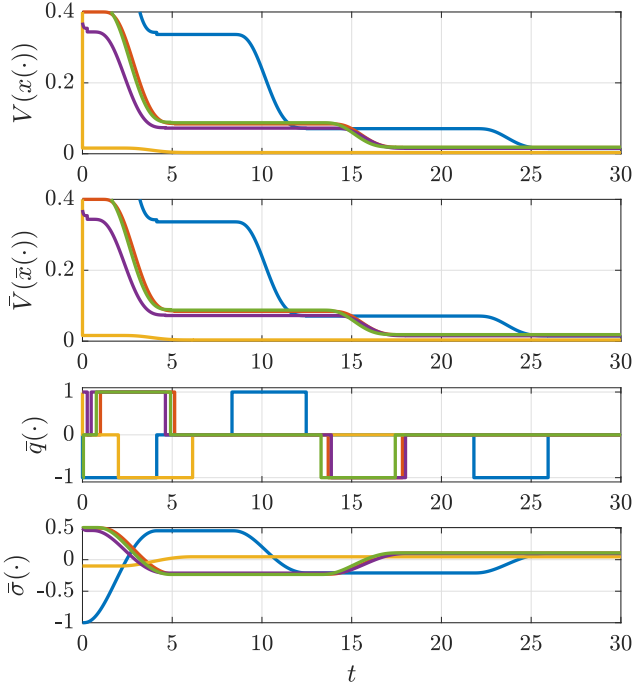


Figure 10: Evolution of the Lyapunov function V in (25) along the solutions represented in Figure 7, and of \bar{V} in (27) evaluated along the associated solutions to (23), as established in Lemma 3.

step of certifying stability of \mathcal{A} under the action of the reset compensation laws.

More specifically, using the tools introduced in this section, we first address in Section 5 the design problem of reset augmentations of the PID control scheme with the goal of transient performance improvement with Coulomb friction. Then, in Section 6, we present a different type of reset PID solution capable of eliminating the hunting behavior and guaranteeing asymptotic stability of the equilibrium set in the presence of Stribeck friction.

5. Reset compensation of Coulomb friction

While we already established in Theorem 1 that the set point is asymptotically stable in the Coulomb friction case of Assumption 1, the slow Lyapunov convergence shown in Figure 10 is associated with undesirably slow transients. As such, the PID controller does not provide satisfactory transient performance. In this section, we first establish rigorously, in Section 5.1, the lack of exponential convergence to \mathcal{A} ; then we present in Section 5.2 the reset PID augmentation proposed in [17], aimed at improving the transient response. While the results of Section 5.2 (and those of [17]) only provide a proof of asymptotic convergence, the increased transient performance with the proposed reset laws is explained and clarified in Section 5.3, where we discuss exponential convergence of a specific set of solutions when represented in suitable coordinates stemming from a generalization of the hybrid automaton representation introduced in Section 4.2.

5.1. Properties not enjoyed by \mathcal{A}

With Coulomb friction, namely under Assumption 1, the main result of [22], summarized in Theorem 1 above, establishes a desirable global asymptotic stability property of the set \mathcal{A} of all equilibria in (18) for the closed loop (6). Nevertheless, the simulations reported in Figure 7 reveal an undesirably slow convergence to \mathcal{A} of the solutions. These long settling times are caused by the depletion and refilling of the integral buffer that is required to overcome the static friction F_s upon overshoot, resulting in a change of sign of the integrator state of the PID controller (see the bottom plot of u_{PID} in Figure 4 or the plot of ϕ in Figure 7). This process is generally slow and takes increasingly more time with a decreasing position error, resulting in long periods of stick and thus a poor transient performance in the sense of settling times. This is also visible from the long intervals when $\bar{q} = 0$ and V (or \bar{V}) remains constant in Figure 10.

Slow convergence is well characterized mathematically by recognizing that the set \mathcal{A} is indeed globally asymptotically stable, but it is not locally exponentially stable, which means that there exists no uniform exponential bound enjoyed by all solutions in any small neighborhood of \mathcal{A} . The lack of local exponential stability has been pointed out in [22, Remark 3] and is recalled here for the reader's convenience. Consider an initial condition $x(0) = (\sigma(0), \phi(0), v(0)) = (\epsilon_k, 0, 0)$ with $\epsilon_k \in (0, F_s)$. Then we have from (19), $|x(0)|_{\mathcal{A}}^2 = \epsilon_k^2$. Since $\epsilon_k < F_s$ and $v = 0$, the initial evolution is in a stick phase, characterized by $\phi(t) = \epsilon_k t$, $\sigma(t) = \epsilon_k$, $v(t) = 0$ for all $t \in [0, T_k] := [0, \frac{F_s}{\epsilon_k}]$ (this is because $\phi(T_k) = F_s$). Then, for a sequence $\{\epsilon_k\}_{k=1}^{\infty}$ with $\epsilon_k \rightarrow 0$ as $k \rightarrow \infty$, we obtain the following sequence of solutions:

$$|x_k(t)|_{\mathcal{A}} = |x_k(0)|_{\mathcal{A}} = \epsilon_k \text{ for all } t \leq T_k, \quad (29)$$

$$\text{with } \lim_{k \rightarrow \infty} \epsilon_k = 0 \text{ and } \lim_{k \rightarrow \infty} T_k = +\infty.$$

Such a sequence of solutions, clearly evolves arbitrarily close to \mathcal{A} and excludes local exponential convergence.

Remark 9. The sequence of solutions constructed in (29) also provides a proof of the fact that the set of equilibria \mathcal{A} does not enjoy the property of pointwise asymptotic stability (PAS), also called semistability (see [40] and references therein). Pointwise asymptotic stability is defined as the property that every point in \mathcal{A} be a Lyapunov stable equilibrium, and that every solution converge to one of the equilibria in the set. The reason why the solutions in (29) disprove the PAS property of \mathcal{A} is that those solutions start arbitrarily close to the origin $x_o := (0, 0, 0) \in \mathcal{A}$, and each one of them reaches the point $x(T_k) = (\epsilon_k, F_s, 0)$ whose Euclidean distance from x_o is larger than F_s . As a consequence, x_o is not Lyapunov stable and PAS does not hold. \lrcorner

This performance deficiency of PID control for motion systems with Coulomb friction inspired us to propose a

PID-based reset control strategy, discussed in the next section.

5.2. Reset PID with time regularization

The slow convergence induced by standard PID control for a motion system with Coulomb friction has been addressed in [17]. Therein, we proposed a *reset* PID control scheme cast in the context of hybrid dynamical systems and strongly inspired by the Lyapunov function (25) (equivalently, its “hybrid” version in (27)). In the design of this reset controller, it has been key noticing that, whenever $\phi v \leq 0$, it is possible to reset the controller state ϕ to any fraction $-\alpha\phi$ (with $\alpha \in [0, 1]$) of its opposite value without experiencing any increase of the Lyapunov function. This reset mechanism is inspired by the intuition that changing the sign of ϕ allows jumping rapidly to the opposite side of the “stick band” (corresponding to the set $\{x \in \mathbb{R}^3: v = 0, |\phi| \leq F_s\}$ in the phase portrait of Figure 7, for example), thereby significantly decreasing the duration of the stick phase, essentially responsible for the slow convergence. Reducing parameter α can then be used as an indication of how cautious this reset action should be (lower α being more cautious) and can help in robustifying the scheme with respect to, e.g., asymmetric friction characteristics.

The exact *reset PID* solution presented in [17] extends the continuous-time model (17) and uses space regularization (namely it inhibits the resets when ϕ is too small) to avoid persistent resets resulting into nonconverging Zeno behavior. In particular, the resets are therein inhibited when $|\phi\sigma|$ is smaller than a space regularization parameter ε . Here, in view of the semiglobal dwell time guarantee established in Lemma 2, we prefer using time regularization; namely, resets are inhibited for some time δ after each reset action. The advantage of this second approach, enabled by the recent intuitions reported in [21], is that it preserves the homogeneity of the jump set. More precisely, a time-regularized version of the design in [21] provides the following reset-augmented version of dynamics (17) (equivalently, (6)):

$$\begin{cases} \dot{x} \in F(x) = \begin{bmatrix} -k_i v \\ \sigma - k_p v \\ \phi - k_d v - F_s \text{Sign}(v) \end{bmatrix} & (x, \tau) \in C, \\ \dot{\tau} = 1 - dz_1(\tau/\delta), \end{cases} \quad (30a)$$

$$\begin{cases} x^+ = g(x) := \begin{bmatrix} \sigma \\ -\alpha\phi \\ v \end{bmatrix} \\ \tau^+ = 0, \end{cases} & (x, \tau) \in D. \quad (30b)$$

In (30), the flow map is inherited from (17) in the Coulomb case of Assumption 1 ($\psi \equiv 0$), and the timer τ is introduced to enforce the time regularization mechanism commented above. The set D , where the resets are triggered, is selected as

$$D := \{(x, \tau) : (\phi\sigma \leq 0) \wedge (\phi v \leq 0) \wedge (\tau \in [\delta, 2\delta])\}, \quad (30c)$$

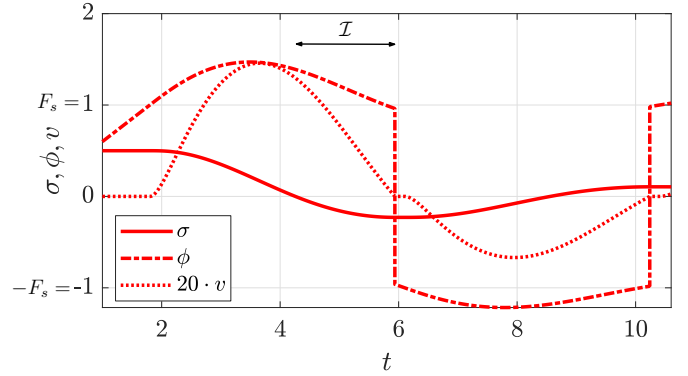


Figure 11: State evolution of (30) illustrating Remark 10. The integrator resets via a sign change of ϕ are clearly visible just before $t = 6$ and just after $t = 10$.

whereas the flow set C is the closure of its complement, namely

$$C := \{(x, \tau) : (\phi\sigma \geq 0) \vee (\phi v \geq 0) \vee (\tau \in [0, \delta])\}. \quad (30d)$$

As specified in Table 1, the simulations reported in this section about the reset-PID feedback (30) focus on the high-performance case $\alpha = 1$. Smaller selections of $\alpha < 1$ lead to increased robustness to asymmetric friction cases. They are discussed in the experiments reported in Section 7.

Remark 10. Let us elaborate on the rationale behind the design of the jump set D using Figure 11. Loosely speaking, we reset ϕ when the solution simultaneously satisfies two conditions: 1) it enters a stick phase (where $v = 0$), and 2) the generalized position σ overshoots the setpoint. A reset of ϕ in such conditions reduces the time needed for the depletion and refilling of the integrator buffer, and consequently the stick duration. Figure 11 illustrates this reset design for the case $\alpha = 1$ (namely $\phi^+ = -\phi$), which is the most representative one. In particular, $\phi v \leq 0$ robustly represents the zero crossing instant for the speed, while $\phi\sigma \leq 0$ only occurs after an overshoot (interval \mathcal{I} in the figure), thereby avoiding resets when stick is reached without overshoot, due to, e.g., different initial conditions, gain tuning, or friction characteristics. \lrcorner

The effectiveness of the reset strategy in (30) can be appreciated in the comparative results of Figure 12, where two solutions (dashed) from Figure 7 (i.e., for the Coulomb friction scenario and without resets) are compared with two solutions (solid) of the closed loop (30), with resets, starting from the same initial conditions and with the same parameters from Table 1. It is apparent from the generalized position σ shown in the top plot, that the convergence time is greatly reduced by the reset actions. This is even more evident from the bottom plot, showing the logarithm of the distance to \mathcal{A} of the state component x . The faster convergence of the solid curves as compared to the dashed ones is clearly visible on a logarithmic scale.

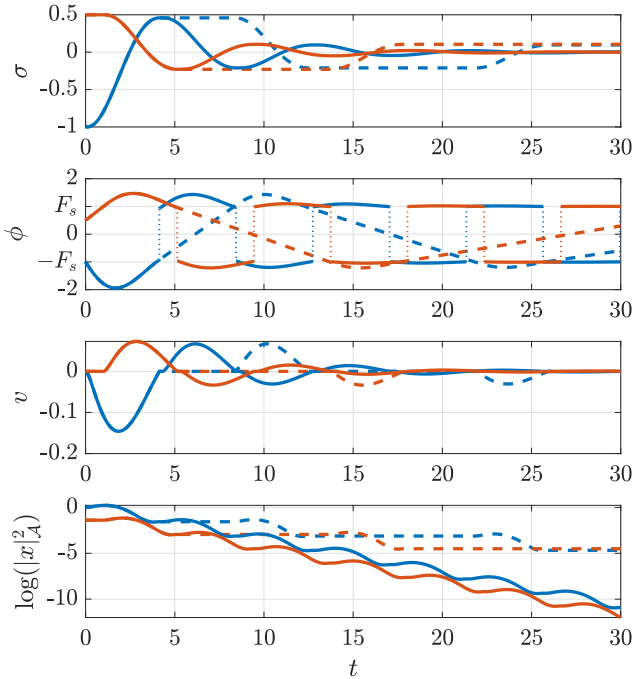


Figure 12: State variables (σ, ϕ, v) and logarithm of $|x|_{\mathcal{A}}^2$ associated with two pairs of solutions (blue and orange), each pair starting from the same initial conditions for the Coulomb scenario with no reset as in (17) (dashed) and with resets as in (30) (solid).

Let us now further explain how the resets enable this transient performance improvement. Comparing the dashed and solid curves in the middle-top plot in Figure 12 it is evident that the jumps of ϕ cause a substantial reduction of the stick phase, thereby inducing faster convergence. A closer inspection of Figure 12 actually reveals that over time the evolution of ϕ converges to a solution resetting between F_s and $-F_s$, thereby precisely compensating for the unknown friction force with the correct magnitude and the correct sign. In Section 5.3, the technical reasons for this behavior of ϕ are explored in greater detail.

Remark 11. The jump set D is expressed in (30c) in terms of x . The states ϕ and σ are not measurable in the case of an unknown mass m , as one can see from (16) and (7). However, even for an unknown mass m , we can define from (16) and (7) the measurable states

$$\sigma_{\circ} := m\sigma = -\bar{k}_i(z_1 - r), \quad (31a)$$

$$\phi_{\circ} := m\phi = -\bar{k}_p(z_1 - r) - \bar{k}_i z_3. \quad (31b)$$

This leads to jump conditions that can be checked based on the measurable states σ_{\circ} and ϕ_{\circ} , in which m does not appear. \lrcorner

The main result of [17] establishes GAS of \mathcal{A} when using the reset mechanism in (30) for the space-regularized solution (without timer τ). The proof is based on the following extension of Proposition 1.

Proposition 3. *Under Assumption 1, for any $\alpha \in [0, 1]$, the Lyapunov-like function V in (25) satisfies all the items of Proposition 1 along dynamics (30), in addition to the jump condition*

$$V(g(x)) - V(x) \leq 0, \quad \text{for all } (x, \tau) \in D.$$

Using Proposition 3, in [17] the Lyapunov-based proof⁶ of Theorem 1 is adapted for proving global \mathcal{KL} asymptotic stability of the extended attractor $\mathcal{A} \times [0, 2\delta]$ for the extended state (x, τ) of the reset dynamics (30) (where $\tau \in [0, 2\delta]$ is essentially a “don’t care” condition). As a matter of fact, resets cannot destroy the Lyapunov decrease and the ensuing proof of the reset-free case of Theorem 1. The next theorem is then the time-regularized parallel result to the space-regularized result in [17]. Its proof exploits the semiglobal properties established in Lemma 3 combined with the properties (28) of the hybrid Lyapunov function \bar{V} in (27).

Theorem 2. *Under Assumption 1, for each $\alpha \in [0, 1]$ and each $\delta > 0$, the compact set $\mathcal{A} \times [0, 2\delta]$ in (18) is globally \mathcal{KL} asymptotically stable for (30) and function V in (25) is non-increasing and converging to zero along all solutions.*

To illustrate Theorem 2, Figure 13 shows the solutions to (30) starting from the same initial conditions as those used in Figure 7 in the absence of resets (the colors are matched for the same initial conditions). The fast convergence to zero of the (squared) distance to $\mathcal{A} \times [0, 2\delta]$ reported in the lower plot clearly illustrates the positive effects of the resets (this was already observed in the lower plot of Figure 12 using a logarithmic scale). An even deeper understanding of the behavior of solutions is visible in Figure 14. This figure shows the evolution of the Lyapunov function V along the same solutions (again, with matching colors), which confirms the results of Proposition 3 and should be compared with the evolution of V along the solutions to (17) (namely, the classical PID closed loop without resets) already reported in Figure 10. Figure 14 also shows the logarithm of V (middle plot) and the reset times for each one of the five simulated initial conditions (bottom plot – again with matching colors). Both these plots seem to suggest that solutions converge exponentially to \mathcal{A} , thereby improving upon the lack of exponential convergence discussed in Section 5.1. These exponential convergence features are discussed in the next section.

5.3. Remarks on local exponential convergence

In this section, we will present a conjecture, with supporting analysis, showing that a highly relevant subset of

⁶To be precise, the Lyapunov-based proof of Theorem 1 given in [22] used continuous-time invariance principles, therefore an alternative parallel proof technique based on hybrid meagre limsup invariance principles was given in [17].

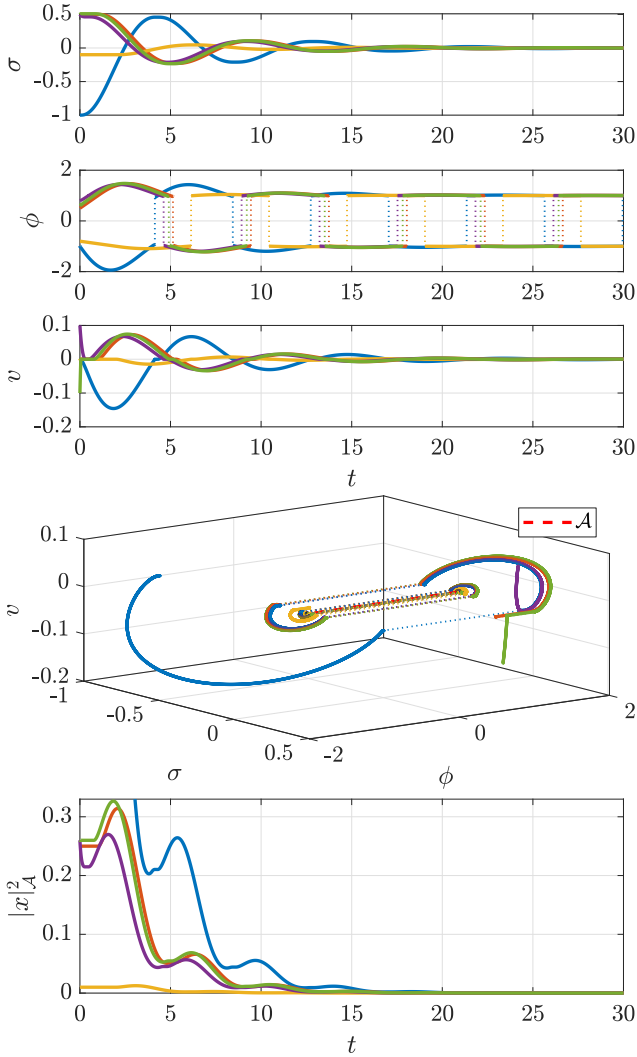


Figure 13: Solutions of (30) from the same initial conditions as those of Figure 7 and the corresponding distance from \mathcal{A} in (19).

solutions to (30) actually converge exponentially fast to the set \mathcal{A} . This provides a partial explanation for the observations on the exponential decay of the Lyapunov function in the previous section and highlights a beneficial performance feature of the proposed reset controller.

Inspecting the simulation results of Figures 13 and 14 a natural question arises about whether the attractor $\mathcal{A} \times [0, 2\delta]$ is actually locally exponentially stable (in addition to globally asymptotically stable, as established in Theorem 2) for the reset-augmented dynamics (30). This intuition is supported by the two bottom plots in Figure 14. The second plot in Figure 14 clearly suggests a linearly decreasing upper bound for $\log(V)$, i.e., a decreasing exponential upper bound for V . The third plot in Figure 14 shows a pseudo-periodic pattern for the reset times along all five simulated solutions (even though the resets are state-triggered), suggesting that the solutions enjoy a desirable homogeneity property where smaller evolutions are scaled versions of the larger ones.

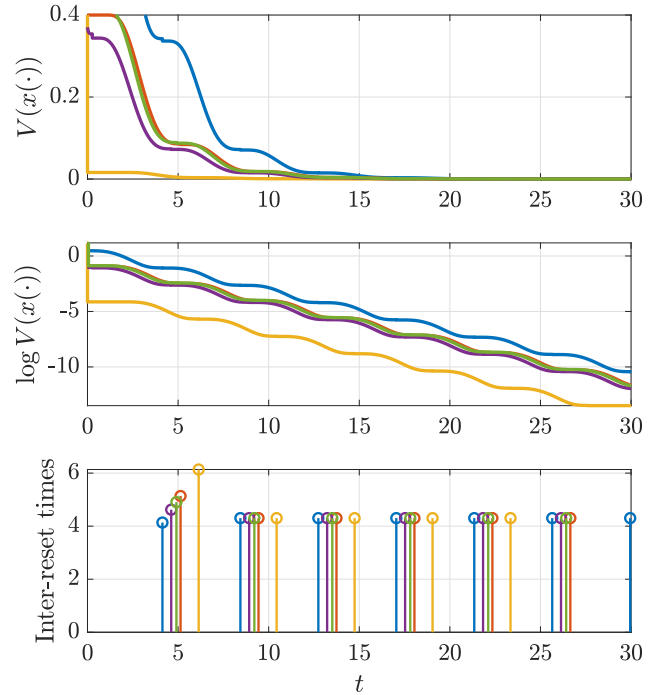


Figure 14: Evolution of function V of (25a) for the solutions to (30) reported in Figure 13 (top). Logarithm of V suggesting exponential convergence (middle), and reset times suggesting homogeneous behavior (bottom).

A fact that was not observed (nor highlighted) in [17] is that, despite the desirable transient performance improvement visible from all the performed simulations, the set $\mathcal{A} \times [0, 2\delta]$ is not locally exponentially stable for (30). The lack of (local) exponential convergence is established by using the sequence of solutions defined in the text before (29). These solutions (augmented with any evolution of the additional state τ) are also solutions to (30), because they belong to the flow set \mathcal{C} in (30d) during their initial stick phase. As a consequence, while the reset strategy in (30) provides very desirable simulation and experimental results (see the experiments in [17]), it does not resolve the lack of (local) exponential stability pointed out in Section 5.1.

A partial explanation of the desirable exponential decay visible in the solutions to (30) represented in Figure 14 is given by introducing a generalized version of the hybrid dynamics (23) stemming from the observation that, when the PID gains selection induces overshoots, the state variable ϕ is never zero along these solutions and always satisfies $\phi v \geq 0$ (see the corresponding traces at the top of Figure 13 and also the traces in Figure 11). Consider then the augmented state

$$\bar{x} \in \bar{\Xi} := \{ \bar{x} = (\bar{\sigma}, \bar{\phi}, \bar{v}, \bar{q}, \bar{\tau}, \bar{a}) \in \mathbb{R}^3 \times \{-1, 0, 1\} \times [0, 2\delta] \times \{-1, 1\} : \bar{a}\bar{\phi} \geq 0, \bar{a}\bar{v} \geq 0 \}, \quad (32a)$$

where we keep the same symbols as in (23a) to avoid making the notation unnecessarily complex. State \bar{x} incorporates the extra logic variable $\bar{a} \in \{-1, 1\}$ satisfying $\bar{a}\bar{\phi} \geq 0$

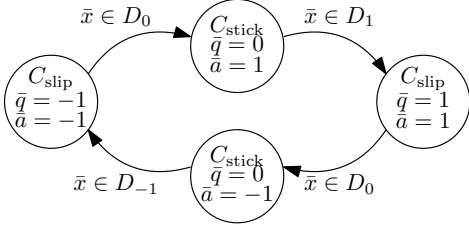


Figure 15: Extended hybrid automaton underlying (32) with the new logical state \bar{a} capturing the alternating speed over consecutive stick-slip transitions.

(and therefore $\bar{a}\bar{\phi} > 0$ along the solutions of interest because neither of them is ever zero) in addition to $\bar{a}\bar{v} \geq 0$ because we observed above that $\phi v \geq 0$.

With this new variable \bar{a} , the automaton of Figure 9 is lifted into the extended automaton shown in Figure 15, which better highlights the fact that stick-slip and slip-stick transitions are characterized in Figure 13 by alternating and consistent signs of \bar{v} and $\bar{\phi}$ (and therefore also of the new variable \bar{a}).

The extended hybrid automaton then corresponds to (23b), (23c) with the extended selections of \bar{f} and \bar{G} ,

$$\bar{f}(\bar{x}) := \begin{bmatrix} -k_i \bar{v} \\ \bar{\sigma} - k_p \bar{v} \\ -k_d \bar{v} + |\bar{q}|(\bar{\phi} - \bar{a}F_s) \\ 0 \\ 1 - \text{dz}_1(\bar{\tau}/\delta) \\ 0 \end{bmatrix}, \quad \bar{G}(\bar{x}) := \bigcup_{i: \bar{x} \in D_i} \{g_i(\bar{x})\}, \quad (32b)$$

where we used the fact that $\psi \equiv 0$ for the Coulomb case. Moreover, the jump maps in (32b) are selected as

$$g_1(\bar{x}) := \begin{bmatrix} \bar{\sigma} \\ \bar{\phi} \\ \bar{v} \\ 1 \\ 0 \\ \bar{a} \end{bmatrix}, \quad g_{-1}(\bar{x}) := \begin{bmatrix} \bar{\sigma} \\ \bar{\phi} \\ \bar{v} \\ -1 \\ 0 \\ \bar{a} \end{bmatrix}, \quad g_0(\bar{x}) := \begin{bmatrix} \bar{\sigma} \\ -\alpha \bar{\phi} \\ \bar{v} \\ 0 \\ \bar{\tau} \\ -\bar{a} \end{bmatrix}, \quad (32c)$$

where we incorporated the reset law (30b) and the toggling of the new logic variable \bar{a} within g_0 , because the jump set in (30c) triggers jumps whenever the automaton of Figure 15 performs a transition from $q \in \{-1, 1\}$ (slip) to $q = 0$ (stick). The description is completed by the next flow and jump sets

$$C_{\text{slip}} := \{\bar{x} \in \bar{\Xi}: |\bar{q}| = 1, \bar{q}\bar{v} \geq 0\} \quad (32d)$$

$$C_{\text{stick}} := \{\bar{x} \in \bar{\Xi}: \bar{q} = 0, \bar{v} = 0, \bar{a}\bar{\phi} \leq F_s\} \quad (32e)$$

$$D_1 := \{\bar{x} \in \bar{\Xi}: \bar{q} = 0, \bar{v} = 0, \bar{a}\bar{\phi} \geq F_s, \bar{\tau} \in [\delta, 2\delta]\} \quad (32f)$$

$$D_{-1} := \{\bar{x} \in \bar{\Xi}: \bar{q} = 0, \bar{v} = 0, \bar{a}\bar{\phi} \geq F_s, \bar{\tau} \in [\delta, 2\delta]\} \quad (32g)$$

$$D_0 := \{\bar{x} \in \bar{\Xi}: |\bar{q}| = 1, \bar{v} = 0, \bar{a}\bar{\phi} \leq F_s\}, \quad (32h)$$

where we emphasize the consistent expressions of C_{stick} , D_1 , D_{-1} and D_0 using the new variable \bar{a} immediately following from (23g)–(23i) together with the constraints on $\bar{\Xi}$ in (32a).

The hybrid dynamics (23b), (23c) with the extended selections (32) can be now represented using the set of

coordinates

$$\hat{x} := (\hat{\sigma}, \hat{\phi}, \hat{v}, \hat{q}, \hat{\tau}, \hat{a}) = (\bar{\sigma}, \bar{\phi} - \bar{a}F_s, \bar{v}, \bar{q}, \bar{\tau}, \bar{a}). \quad (33a)$$

Coordinates (33a) intentionally disregard the “stick” strip corresponding to the flat region in the phase portrait of Figure 13 where $|\bar{\phi}| \leq F_s$, by way of the shifted state variable $\bar{\phi} - \bar{a}F_s$, where \bar{a} toggles between ± 1 . These new coordinates are easily shown to satisfy the following transformed version of dynamics (23b), (23c), (32) (where we used $\bar{a}^2 = 1$)

$$\begin{cases} \dot{\hat{x}} = \hat{f}(\hat{x}), & \hat{x} \in \hat{C} := \hat{C}_{\text{slip}} \cup \hat{C}_{\text{stick}} \\ \hat{x}^+ \in \hat{G}(\hat{x}), & \hat{x} \in \hat{D} := \bigcup_{i \in \{1, -1, 0\}} \hat{D}_i \end{cases} \quad (33b)$$

$$\hat{f}(\hat{x}) := \begin{bmatrix} -k_i \hat{v} \\ \sigma - k_p \hat{v} \\ -k_d \hat{v} + |\hat{q}| \hat{\phi} \\ 0 \\ 1 - \text{dz}_1(\hat{\tau}/\delta) \\ 0 \end{bmatrix}, \quad \hat{G}(\hat{x}) := \bigcup_{i: \hat{x} \in \hat{D}_i} \{\hat{g}_i(\hat{x})\}, \quad (33c)$$

$$\hat{g}_1(\hat{x}) := \begin{bmatrix} \hat{\sigma} \\ \hat{\phi} \\ \hat{v} \\ 1 \\ 0 \\ \hat{a} \end{bmatrix}, \quad \hat{g}_{-1}(\hat{x}) := \begin{bmatrix} \hat{\sigma} \\ \hat{\phi} \\ \hat{v} \\ -1 \\ 0 \\ \hat{a} \end{bmatrix}, \quad \hat{g}_0(\hat{x}) := \begin{bmatrix} (1-\alpha)\bar{a}F_s - \alpha\hat{\phi} \\ \hat{v} \\ 0 \\ \hat{\tau} \\ -\hat{a} \end{bmatrix}$$

$$\hat{C}_{\text{slip}} := \{\hat{x}: |\hat{q}| = 1, \hat{q}\hat{v} \geq 0\} \quad (33d)$$

$$\hat{C}_{\text{stick}} := \{\hat{x}: \hat{q} = 0, \hat{v} = 0, \hat{a}\hat{\phi} \leq 0\} \quad (33e)$$

$$\hat{D}_1 := \hat{D}_{-1} := \{\hat{x}: \hat{q} = 0, \hat{v} = 0, \hat{a}\hat{\phi} \geq 0, \hat{\tau} \in [\delta, 2\delta]\} \quad (33f)$$

$$\hat{D}_0 := \{\hat{x}: |\hat{q}| = 1, \hat{v} = 0, \hat{a}\hat{\phi} \leq 0\}. \quad (33g)$$

The interesting feature of dynamics (33) is that with the exception of the second entry in \hat{g}_0 , all the flow and jump maps and the flow and jump sets are partially homogeneous in the coordinates $(\hat{\sigma}, \hat{\phi}, \hat{v})$. This property also applies to the second entry of \hat{g}_0 for the special case $\alpha = 1$, which implies $(1 - \alpha)\bar{a}F_s = 0$. We then have the next property.

Lemma 4. *Select $\alpha = 1$. For any solution $\hat{x} = (\hat{\sigma}, \hat{\phi}, \hat{v}, \hat{q}, \hat{\tau}, \hat{a})$ of dynamics (33) and any $\lambda > 0$, function $\hat{x}_\lambda := (\lambda\hat{\sigma}, \lambda\hat{\phi}, \lambda\hat{v}, \hat{q}, \hat{\tau}, \hat{a})$ is a solution too.*

Exploiting the homogeneity property of Lemma 4 and the fact that the two hybrid models (23b), (23c), (32) and (33) provide representations of the solutions to (30), we may better understand and characterize the exponential decrease that we had noticed in the time histories of Figure 12, in addition to the desirable property (also visible in Figure 13) that the norm of the state variable ϕ asymptotically converges to F_s , with the actual variable ϕ toggling persistently (and homogeneously) between its positive and negative estimate. We recall that this fact (ϕ converging to the unknown F_s in a resetting fashion and immediately compensating for it since it represents the proportional-integral action of the controller) was already observed in

the simulations in Section 5.2. More specifically, we reach the following conjecture, whose proof would be lengthy and is left as future work along the main steps provided in the sketch below.

We emphasize that an assumption is made in the conjecture below about a specific set of solutions under consideration, both in terms of their initial conditions and their evolution. While this condition might be hard to check theoretically, we emphasize that in many of the simulations shown in this paper (and experienced experimentally) we exactly see these types of solutions, which hopefully provides a convincing argument about the relevance of this statement.

Conjecture 1. *Consider system (30) with $\alpha = 1$ and assume that the set of solutions starting at the beginning of a slip phase (namely, with $x(0, 0) = (\sigma(0, 0), \phi(0, 0), v(0, 0)) = (\sigma_0, F_s \text{sign}(\sigma_0), 0)$ for any $\sigma_0 \neq 0$) are characterized by alternating positive/negative slip to stick transitions with ϕ never vanishing. Then those solutions converge uniformly and exponentially, namely there exist $M > 0$ and $\mu > 0$ such that*

$$\left\| \begin{bmatrix} \sigma(t, j) \\ \phi(t, j) - \text{sign}(\phi(t, j))F_s \\ v(t, j) \end{bmatrix} \right\| \leq Me^{-\mu t} |\sigma_0|. \quad (34)$$

Moreover, $|\phi(t, j)|$ converges exponentially to F_s .

Sketch of the proof. While a careful and complete proof of Conjecture 1 is beyond the scope of this note, we believe that most of the necessary tools are well summarized in this section. In particular, a first step should involve a formal proof of the fact that the solutions of (23b), (23c), (32) are a representation of the solutions to (30) (in the sense of Lemma 3) for the initial conditions specified in the statement. Then the GAS result of Theorem 2 implies that solutions to (23b), (23c), (32) (equivalently (33)) converge to a bounded set, and finally this means from Lemma 4 that solutions converge exponentially and uniformly to zero (homogeneity indeed can be used to show uniform exponential convergence as in [42] or also [79, §IV.A]). The exponential bound (34) then is carried over from the hybrid automaton (33) to the original model (30) due to the representation properties established in the first step. Moreover, by assumption the solutions under consideration start at $\left[\begin{bmatrix} \sigma(0, 0) \\ \phi(0, 0) - \text{sign}(\phi(0, 0))F_s \\ v(0, 0) \end{bmatrix} \right] = \left[\begin{bmatrix} \sigma_0 \\ 0 \\ 0 \end{bmatrix} \right]$, which explains the right-hand side in (34). Note also that the dwell time enjoyed by the dynamics enables transforming any $(t + j)$ exponential bound into a bound only involving the t direction. Finally, since $|\hat{\phi}(t, j) - \hat{a}(t, j)F_s| = |\phi(t, j) - \text{sign}(\phi(t, j))F_s|$ converges exponentially to zero (where $\phi(t, j)$ is never zero), this implies that $|\hat{\phi}(t, j)|$ converges exponentially to F_s . ■

Conjecture 1 captures the main intuition behind the reset PID solution of [17] reported in (30). Loosely speaking, the essential effect of the reset mechanism is to force

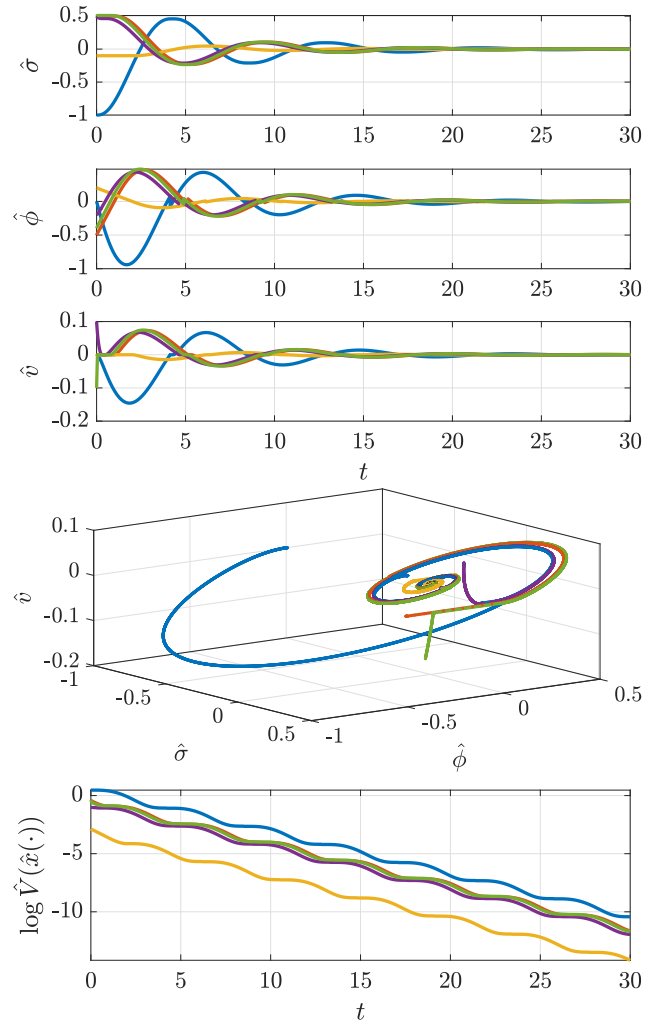


Figure 16: Solutions of (33) from initial conditions corresponding to those of Figure 13 and the corresponding value of the quadratic Lyapunov-like function \hat{V} satisfying (35).

solutions to jump across the “stick band” $\mathcal{E}_{\text{stick}}$ (the flat region in the phase portrait of Figure 13), as indicated by the jumps (dotted) in Figure 13. This transforms the dynamics into a homogeneous behavior emerging from patching together the two “slip” half spaces $\mathcal{E}_{\text{slip}}$ (the tilted regions in the phase portrait of Figure 13).

Figure 16 shows the hybrid representation of the solutions shown in Figure 13 using the alternative coordinates $(\hat{\sigma}, \hat{\phi}, \hat{v})$. Observe the desirable linear-like exponentially converging aspect of the ensuing transients, revealing the successful effect of the reset PID compensation. In fact, the actual dynamics obeys a nontrivial switching mechanism between (short) stick phases and slip behavior: a mechanism that is necessary for compensating the unknown static friction level F_s . The bottom plot of Figure 16 shows the evolution of the logarithm of the quadratic function $\hat{V}(\hat{x}) := \begin{bmatrix} \hat{\sigma} \\ \hat{\phi} \\ \hat{v} \end{bmatrix}^\top P \begin{bmatrix} \hat{\sigma} \\ \hat{\phi} \\ \hat{v} \end{bmatrix}$, with P defined in (25b). It is straightforward to show that this function

satisfies

$$\langle \nabla \hat{V}(\hat{x}), \hat{f}(\hat{x}) \rangle = -c\hat{v}^2, \quad \forall \hat{x} \in \hat{C}_{\text{slip}} \cup \hat{C}_{\text{stick}} \quad (35a)$$

$$\hat{V}(g) - \hat{V}(\hat{x}) \leq 0, \quad \forall \hat{x} \in \hat{D}, \forall g \in \hat{G}(\hat{x}), \quad (35b)$$

along dynamics (33), where $c := 2(k_p k_d - k_i) > 0$ was introduced in Proposition 1. In particular, it is evident that the evolution of the logarithm of \hat{V} at the bottom of Figure 16 mimics the corresponding evolution for function V in (25), reported at the bottom of Figure 14.

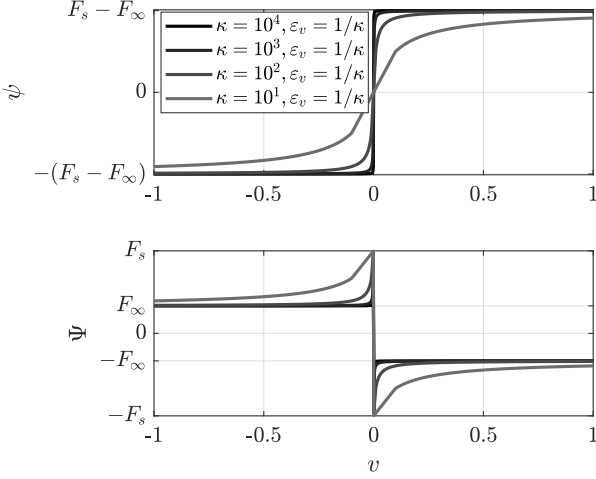


Figure 17: Function ψ given in (15) with increasing values of κ and decreasing values of ϵ_v , and corresponding graph of Ψ in (6b).

6. Reset compensation of Stribeck friction

6.1. Lyapunov-based understanding of hunting

It is commonly acknowledged that the so-called “velocity weakening” shape of the friction nonlinearity Ψ is the key characteristic of Stribeck friction that causes instability and the oscillatory response called hunting. In particular, as visible in the red curve of Figure 3, or in the lower diagram of Figure 17, as the magnitude of the velocity increases from zero, the magnitude of the friction force “weakens”. Simulating model (23) it is possible to understand the net effect of the velocity weakening: at a stick-to-slip transition the control force exactly compensates for the static friction F_s . Immediately after this transition the friction force u_f decreases (due to the velocity weakening characteristic of Stribeck friction) and the control action dramatically overcompensates the friction. The latter induces a highly accelerated motion leading to overshoot. This mechanism ultimately leads to the oscillatory (hunting) response.

To better understand the instability described above, we consider the prototypical Stribeck effect shown in Figure 17 (corresponding to equation (15)) for increasing values of κ and decreasing values of ϵ_v (for example satisfying $\epsilon_v \leq 1/\kappa$ as $\kappa \rightarrow +\infty$). Figure 18 shows the position error

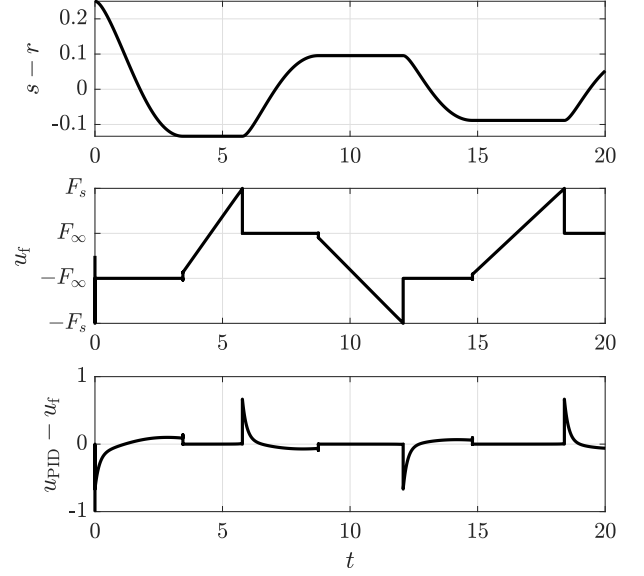


Figure 18: Typical evolution of the position error (top), the friction force (middle) and the net forces acting on the mass with the steepest (darkest) Stribeck function in Figure 17.

$s - r$, the friction force u_f and the net force $u_{\text{PID}} - u_f$ acting on the mass for the friction curves of Figure 17, clearly showing that the friction force drop becomes increasingly abrupt as κ increases.

The limiting shape, corresponding to the darkest curve in Figure 17, resembles a Coulomb friction contribution with amplitude F_∞ away from zero, but a larger value of static friction $F_s > F_\infty$ that must be overcome by the control input to exit a stick phase, thus causing a discontinuous drop of the friction force in Figure 18 at any stick-to-slip transition. This limiting phenomenon can be effectively modeled by adapting the hybrid automaton (23) with the flow map \bar{f} of (23d) replaced by the following selection:

$$\bar{f}(\bar{x}) = \begin{bmatrix} -k_i \bar{v} \\ \bar{\sigma} - k_p \bar{v} \\ -k_d \bar{v} + |\bar{q}| \bar{\phi} - \bar{q} F_\infty \\ 0 \\ 1 - \text{dz}_1(\bar{\tau}/\delta) \end{bmatrix}. \quad (36)$$

Such an adaptation accounts for the fact that the value of $|\Psi(v)|$ when $v \neq 0$ is now F_∞ instead of F_s . Instead, the quantity characterizing the stick and slip sets ($q = 0$ or $|q| = 1$, respectively) in (23f)–(23j) remains unchanged and equal to F_s because in Figure 17 we clearly see that ϕ must overcome F_s exit a stick phase (namely to compensate for the static component of the friction when $v = 0$).

Simulating model (23), (36) we may further understand the net effect of the velocity weakening by inspecting the evolution of the following adaptation of the smooth function in (27),

$$\bar{V}_\infty(\bar{x}) := \begin{bmatrix} \bar{\sigma} \\ \bar{v} \end{bmatrix}^\top \begin{bmatrix} k_d & -1 \\ -1 & k_p \end{bmatrix} \begin{bmatrix} \bar{\sigma} \\ \bar{v} \end{bmatrix} + |\bar{q}| (\bar{\phi} - \bar{q} F_\infty)^2 + (1 - |\bar{q}|) (\text{dz}_{F_\infty}(\bar{\phi}))^2, \quad (37)$$

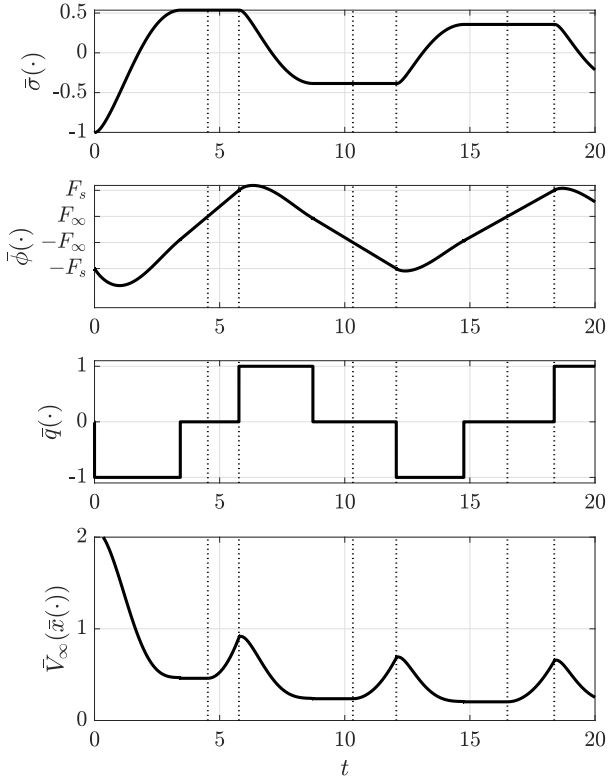


Figure 19: Evolution of the Lyapunov function \bar{V} in (37) along the solutions to (23), (36) and corresponding values of \bar{q} , $\bar{\phi}$ and $\bar{\sigma}$ with the steepest (darkest) Stribeck function in Figure 17.

whose evolution is reported in Figure 19. In particular, it is immediate to verify that properties (28) are still satisfied by \bar{V}_∞ along the solutions to (23), (36), except for the flowing intervals in C_{stick} when $|\bar{\phi}| \in (F_\infty, F_s)$ (corresponding to the intervals marked by the dotted vertical lines in Figure 19).

Since both $\bar{\sigma}$ and \bar{v} are constant during those stick intervals, one can well interpret this phenomenon as an injection of energy into the Lyapunov function caused by the ramping up of $|\bar{\phi}|$ from F_∞ to F_s , as illustrated in the middle-top plot of Figure 19. This increase of \bar{V}_∞ is subsequently compensated by the quasi-homogeneous decrease of \bar{V}_∞ happening in the follow-up slip phase, where $v \neq 0$ introduces dissipation from (28a).

This interplay between injected and dissipated energy can be proven to always lead to the occurrence of a non-trivial attractive hybrid periodic orbit by following similar steps to those reported in [23] (see also [53]). While a rigorous proof of this energy-based explanation of the hunting phenomenon is beyond the scope of this paper, the key mechanism behind it is that the injection of energy is always constant and equal to $(F_s - F_\infty)^2$ (due to the second line of (37)), whereas the dissipated energy during the flow phase is proportional to the value of $\bar{\sigma}$ at the stick-to-slip transition. Indeed, with a larger $|\bar{\sigma}|$ at the stick-to-slip transition we obtain a larger velocity response v and thus a more significant decrease of \bar{V}_∞ . Instead with a smaller

$|\bar{\sigma}|$ at the stick-to-slip transition, the velocity v is smaller and the decrease of \bar{V}_∞ is arbitrarily small. As a result, there exists a critical value of $|\bar{\sigma}|$ (at the stick-to-slip transition) such that the dissipated energy is equal to the injected energy, characterizing an attractive periodic hybrid motion (a hybrid periodic orbit) associated to the hunting phenomenon.

While this analysis is carried out for the limiting case of $\varepsilon_v = 1/\kappa \rightarrow 0$, the essential closed-loop behavior shown in Figure 18 is qualitatively the same also for more realistic values of these parameters.

6.2. Stribeck effects vs Coulomb ones

We illustrate here the fact that the Stribeck-induced problem addressed in this section is substantially different from the Coulomb problem solved in Section 5. In particular, the reset control strategy of Section 5 does not provide a solution for solving the hunting problem (i.e., for stabilizing the unstable setpoint). Indeed, as established in Theorem 1, the closed loop with Coulomb friction enjoys stability of the setpoint, but suffers from long settling times. The reset controller of Section 5 then improves the performance by reducing the settling times. Systems with Stribeck friction, instead, do not enjoy stability of the setpoint, so the control problem must address stabilization. While the reset strategy of Section 5 well compensates the long depletion and refilling phases of the integral state ϕ , it is not designed to compensate for the energy injection experienced at each stick-to-slip transition (as illustrated by the analysis in Section 6.1 and Figure 19).

A confirmation of this fact arises from applying the reset control strategy of Section 5 also to the Stribeck case. The resulting responses show successful compensation of the long filling phases for the integral state ϕ , but are not designed to stabilize the setpoint nor to compensate for the energy injection experienced at each stick-to-slip transition. A confirmation of this fact is shown in Figure 20, which depicts the solutions of the reset-compensated closed loop (30) with F in (30a) replaced by

$$F(x) = \begin{bmatrix} -k_i v \\ \sigma - k_p v \\ \phi - k_d v - F_s \text{Sign}(v) + \psi(v) \end{bmatrix}, \quad (38)$$

namely with the extra Stribeck velocity weakening term $\psi(v)$ of (15) (we use here the parameters in Table 1) that was missing in the Coulomb case of (30a). From the evolution of σ and of the Lyapunov function $\bar{V}_\infty(\bar{x}(\cdot))$ in Figure 20 we can observe that the resetting mechanism works as expected in reducing significantly the stick phases where the reset-free simulations of Figure 19 showed a constant value of $\bar{V}_\infty(\bar{x}(\cdot))$. Nevertheless the fundamental interplay of energy injection/dissipation highlighted in the previous section is still present and clearly visible by the oscillatory behavior of the Lyapunov function (lower plot of Figure 20), where \bar{V}_∞ increases during stick and decreases

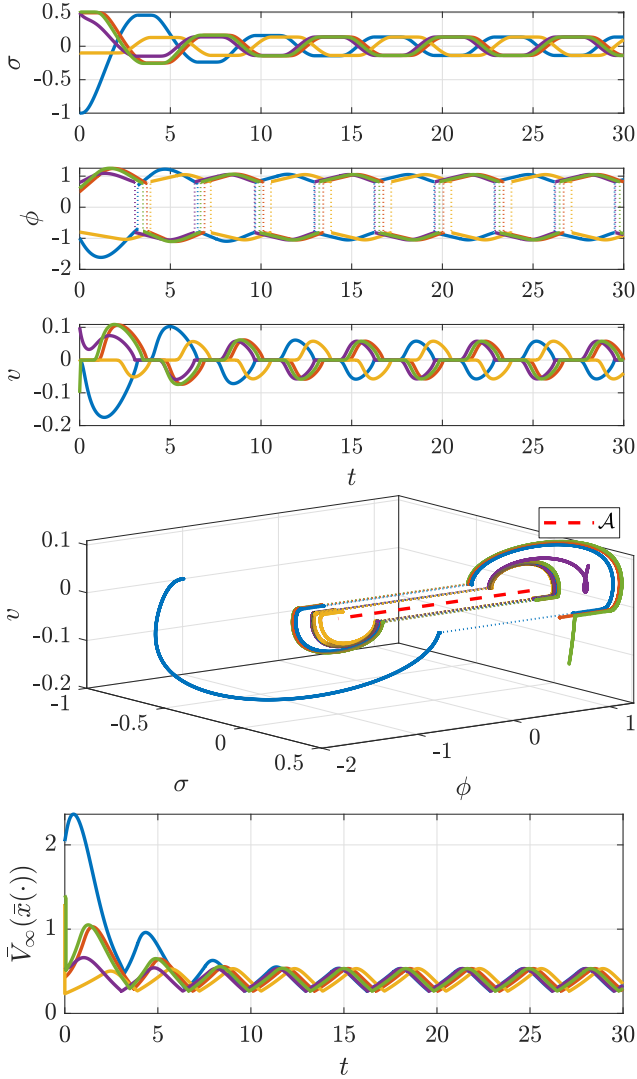


Figure 20: The Coulomb-based reset PID solution of Section 5 reduces the stick phases in the presence of Stribeck friction but does not eliminate the hunting instability. Function \bar{V} is defined in (37).

during slip. In the next section, we present a different resetting logic resolving this instability, taken from our recent work [18].

6.3. Two-steps reset PID law

An effective reset PID solution solving the hunting phenomenon is proposed in our recent work [18]. The key idea is based on the preliminary observation that hunting is associated to alternating zero crossings of σ and v (see the time histories of Figure 8). Then we may proceed as follows:

1. similar to variable \bar{a} of Section 5.3, we augment the controller state with an extra logical variable $b \in \{-1, 1\}$ toggling with the alternating zero crossings of σ and v ; to suitably keep track of this toggling, we impose the constraint $bv\sigma \geq 0$ on variable b ;

2. we impose two different types of jump laws on the (generalized) controller state ϕ , whose net effect is to ensure that the constraint $\sigma\phi \geq \frac{k_p}{k_i}\sigma^2$ is always satisfied. We note that this constraint is equivalent to $(s-r)x_c \geq 0$ in the original coordinates z (see (6) and (16)), namely that the integrator state x_c always points in the same direction as the position error $s-r$. As a consequence, we also impose $bv\phi \geq 0$ so that even when $\sigma = 0$, bv and ϕ must have matching signs.

The interesting feature emerging from the mechanism described above is that, unlike our “simple” Coulomb-oriented solution of Section 5, algebraic restrictions are imposed on certain state variables during in the description of the reset-PID controlled motion system. More specifically, using once again symbols x, σ, v and ϕ to avoid heavy notation, the overall state of the controlled motion system corresponds to

$$\xi := (x, b) := (\sigma, \phi, v, b) \in \Xi \quad (39a)$$

$$\Xi := \{(x, b) \in \mathbb{R}^3 \times \{-1, 1\} : bv\sigma \geq 0, \sigma\phi \geq \frac{k_p}{k_i}\sigma^2, bv\phi \geq 0\}.$$

These constraints on the control variables ϕ and b are implicitly satisfied along the solutions, as long as the controller states are suitably initialized.

To ensure that constraints (39a) are respected (and that the hunting instability is removed), the two jump laws that we implement are triggered by the alternating zero crossings of σ and v according to the following rules:

- when σ crosses zero (which happens when $b = 1$ because σ^2 is decreasing if and only if $0 \geq \sigma\dot{\sigma} = -\sigma k_i v$, that is $b = 1$), both b and ϕ jump to their opposite value (i.e., $b^+ = -b$ and $\phi^+ = -\phi$), so that the constraints of Ξ are preserved;
- when v crosses zero (which happens when $b = -1$ because ϕ^2 is decreasing only if $0 \geq v\phi$, which implies $b = -1$), b is toggled once again to preserve the constraints of Ξ and ϕ is reset to $\phi^+ = \frac{k_p}{k_i}\sigma$, the smallest possible amplitude satisfying the constraints of Ξ .

Let us now formalize more precisely the equations of the PID controlled plant (17) with the extra logical state b and the above described two-fold reset mechanism. Using the state in (39a), we may write the hybrid dynamics as follows:

$$\dot{\xi} \in \begin{bmatrix} -k_i v \\ \sigma - k_p v \\ \phi - k_d v - F_s \text{Sign}(v) + \psi(v) \\ 0 \end{bmatrix}, \quad \xi \in \mathcal{C} := \Xi \quad (39b)$$

$$\xi^+ = \begin{cases} g_\sigma(\xi), & \text{if } \xi \in \mathcal{D}_\sigma \\ g_v(\xi), & \text{if } \xi \in \mathcal{D}_v, \end{cases} \quad \xi \in \mathcal{D} := \mathcal{D}_\sigma \cup \mathcal{D}_v,$$

where the jump maps and jump sets are given by (the subscript “ σ ” or “ v ” indicates whether we are focusing on

the zero crossing of σ or v)

$$g_\sigma(\xi) := \begin{bmatrix} \sigma \\ \phi \\ -b \end{bmatrix}, \quad g_v(\xi) := \begin{bmatrix} \sigma \\ \frac{k_p}{k_i} \sigma \\ v \\ -b \end{bmatrix}, \quad (39c)$$

$$\mathcal{D}_\sigma := \{\xi \in \Xi : \sigma = 0, b = 1\}, \quad (39d)$$

$$\mathcal{D}_v := \{\xi \in \Xi : v = 0, b = -1\}. \quad (39e)$$

Note that the jump map in (39b) is well defined because the two sets \mathcal{D}_σ and \mathcal{D}_v are disjoint (they involve different values of state b).

Remark 12. We mentioned above that in the original coordinates z (see (16)), constraint $\sigma\phi \geq \frac{k_p}{k_i}\sigma^2$ is equivalent to $(s-r)x_c \geq 0$, namely the integrator state x_c always points in the same direction as the position error $s-r$. This behavior is inspired by, and resembles the reset control logic of the so-called Clegg integrator [31, 86]. The difference between our solution and the one of Clegg is in the specific resetting law, where Clegg would merely reset x_c to zero at the zero crossing of $s-r$ (equivalently, of σ). Instead our logic reverses the value of ϕ , which corresponds to $x_c^+ = -x_c$ because $\sigma = 0$ at those jump times.

A partial motivation for the resetting mechanism $\phi^+ = \frac{k_p}{k_i}\sigma$ at the zero crossing of v can be understood once again by studying its effect in the original coordinates z in (6). In particular, since $\dot{x}_c = s-r$ and $x_c(s-r) \geq 0$, one clearly obtains $\frac{d}{dt}|x_c| = |s-r|$ along flowing solutions, which could possibly lead to an unbounded growth of x_c . Moreover, we just observed that $|x_c|$ remains unchanged when jumping at the zero crossing of σ . Then a mechanism is necessary for reducing the norm x_c during the hybrid evolution, which otherwise would be a non-decreasing function of time. Such a mechanism is exactly triggered by the jump $\phi^+ = \frac{k_p}{k_i}\sigma$ imposed at the zero crossing of v , which corresponds to $x_c^+ = 0$ when translated to the original coordinates.

By the above interpretation, it is now clear that the proposed resetting strategy is an essential sophistication of Clegg's original mechanism. Indeed, instead of resetting to zero the integrator state x_c at the zero crossing of the position error $s-r$, we reverse the integrator state at that zero crossing and then we reset it to zero at the subsequent zero crossing of the speed v . A fair question to pose is whether applying the original mechanism of Clegg would result in a stabilizing action. A partial answer to this question is given by the experimental results reported later in Section 7.3, but a rigorous study of this solution has not been carried out yet and is subject of future work. \square

An important question that arises is whether the constraints imposed by Ξ in (39a) on the (continuous and discrete) evolution of the resetting solutions of closed loop (39) still allow (maximal) solutions to be defined for arbitrarily large times (namely whether maximal solutions are complete). The positive answer is established in the next lemma, proven in [18, Prop. 1], which also proves important regularity conditions of the hybrid system data,

ensuring robustness of stability and compactness of the solutions set (see [41, Ch. 5-7] for details).

Lemma 5. *Hybrid system (39) satisfies the hybrid basic conditions of [41, As. 6.5]. Moreover, under Assumption 2, all maximal solutions are complete.*

Since we introduced the additional state variable $b \in \{-1, 1\}$, the stability properties of \mathcal{A} in (18) (equivalently (9)) should be studied by focusing on the extended compact set

$$\mathcal{A}_e := \mathcal{A} \times \{-1, 1\} = \{\xi \in \Xi : \sigma = v = 0, |\phi| \leq F_s\}. \quad (40)$$

comprising all possible equilibria of dynamics (39). The main result of [18, Prop. 1] is summarized by the following clean statement which follows from combining the global asymptotic results of [18, Thm. 1] with the equivalent stability properties established in [41, Thm. 7.12].

Theorem 3. *Under Assumption 2, the set \mathcal{A}_e in (40) is globally \mathcal{KL} asymptotically stable for (39).*

When running simulations and experiments of the reset-PID solution of (39), a possible issue emerges due to the fact that sets \mathcal{D}_σ and \mathcal{D}_v are "thin sets" because they require checking a zero value of the speed v or the position σ . It is however established in [18, Prop. 2] that, as long as state ϕ is not initialized at zero, no solution ever reaches a point where $\phi = 0$. Then, in view of the constraints on Ξ listed in (39a), a numerically robust version of the jump sets \mathcal{D}_σ and \mathcal{D}_v is given by the alternative selection

$$\mathcal{D}_\sigma^r := \{\xi : \sigma\phi \leq 0, b = 1\} \quad (41)$$

$$\mathcal{D}_v^r := \{\xi : v\phi \geq 0, b = -1\}, \quad (42)$$

which satisfy $\mathcal{D}_\sigma^r \cap \Xi_0 = \mathcal{D}_\sigma \cap \Xi_0$ and $\mathcal{D}_v^r \cap \Xi_0 = \mathcal{D}_v \cap \Xi_0$, with $\Xi_0 := \{\xi \in \Xi : \phi = 0\}$. Using these selections, we have run a set of simulations of (39) from the same initial conditions reported in Figures 8, 19 and 20. The resulting solutions show the desirable convergence properties established in Theorem 3 and are reported in Figure 21. From the bottom plot it is apparent that the distance to \mathcal{A}_e converges to zero, as established in Theorem 3, but it is also evident that the convergence is not exponential, due to the increasingly long stick phases characterizing the convergence transient.

6.4. Semiglobal dwell time and hybrid extended model

The proof of Theorem 3 given in [18] is carried out by relying on a generalization of the hybrid extended model introduced in Section 4.2. In particular, following similar steps to those of Section 4.2, we may establish a semiglobal dwell-time property parallel to the one of Lemma 2, suitably stated by introducing the following generalized version of the incipient slip sets of (22), where we now include the new state variable b ,

$$\mathcal{S}_1 := \{\xi \in \Xi : \phi \geq F_s, v = 0, b = 1\}, \quad (43)$$

$$\mathcal{S}_{-1} := \{\xi \in \Xi : \phi \leq -F_s, v = 0, b = 1\}.$$

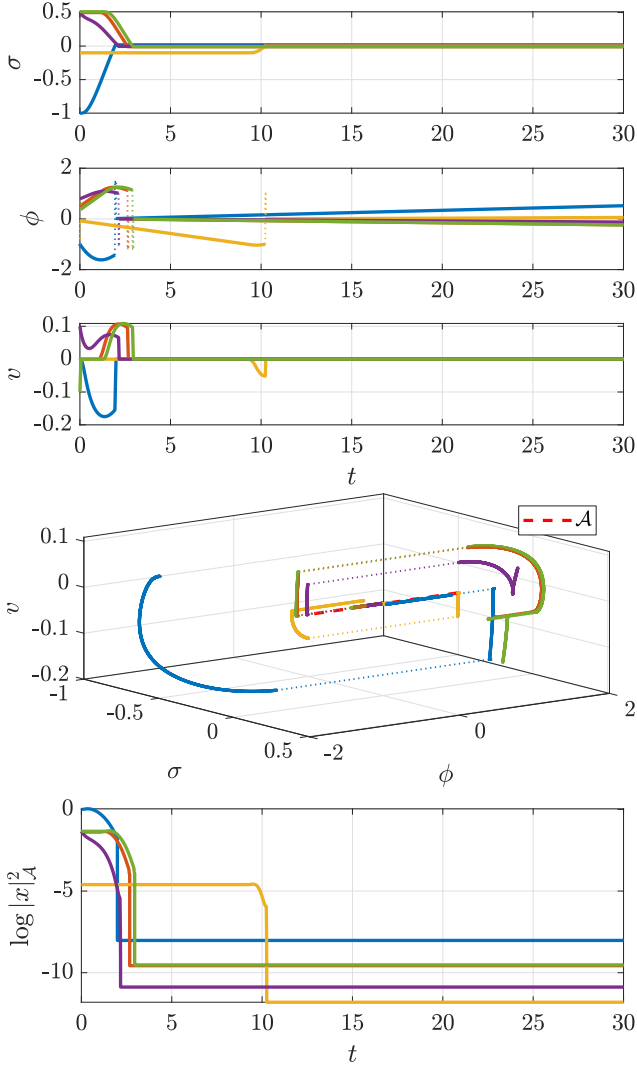


Figure 21: Solutions of (39) from the initial conditions of Figure 8 and logarithm of the corresponding (squared) distance of $\xi = (x, b)$ from \mathcal{A}_e in (40), which is equivalent to $|x|_{\mathcal{A}}$ with \mathcal{A} in (18).

The next lemma, paralleling Lemma 4.2 but for the reset-augmented system (39), shows that any solution visiting the sets in (43) enjoys a uniform semiglobal dwell time before its velocity changes sign, unless it reaches the attractor \mathcal{A}_e , where it will remain forever. Its proof comes from combining the results in [18, Prop. 3(i)] and [18, Prop. 5].

Lemma 6. *Under Assumption 2, for each compact set \mathcal{K} , there exists $\delta(\mathcal{K}) > 0$ such that each solution $\xi = (\sigma, \phi, v, b)$ of (39) starting in \mathcal{K} satisfies the following. For any $(t, j) \in \text{dom } \xi$ such that $\xi(t, j) \in \mathcal{S}_1 \cup \mathcal{S}_{-1}$, then either $\xi(t', j') \in \mathcal{A}_e$ for some $t' \in [t, t + \delta(\mathcal{K})]$, and the solution remains in \mathcal{A}_e for all subsequent times, or otherwise it*

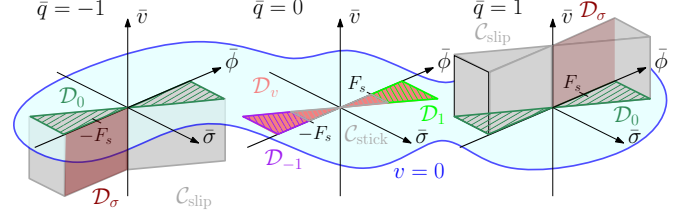


Figure 22: Projections to the $(\bar{\sigma}, \bar{\phi}, \bar{v})$ space of the flow and jump sets in (44f), indicating the sector condition $\bar{\sigma}\bar{\phi} \geq \frac{k_p}{k_i}\bar{\sigma}^2$.

holds⁷ that $(s, j(s)) \in \text{dom } \xi$ and

$$\begin{aligned} \xi(t, j) \in \mathcal{S}_1 &\implies v(s, j(s)) \geq 0, \\ \xi(t, j) \in \mathcal{S}_{-1} &\implies v(s, j(s)) \leq 0, \end{aligned}$$

for all $s \in [t, t + \delta(\mathcal{K})]$.

Remark 13. It is interesting to observe that, differently from Lemma 2, the proof of Lemma 6 requires proving a preliminary boundedness result (stated in [18, Prop. 4]) whose proof is not straightforward, due to the presence of the reset actions, which make it not possible to follow the same simple BIBO reasoning reported in Remark 7. \square

Similar to Section 4.2, based on Lemma 6, we may now introduce a hybrid extended model capable of semiglobally representing dynamics (39). The extended hybrid model enables constructing a Lyapunov functions to prove Theorem 3 and is parametrized by quantity δ from Lemma 6.

To this end, just as before, we augment the state ξ with a logical variable \bar{q} and with a timer $\bar{\tau}$ so that the augmented state inherits the constraints of Ξ in (39a) and corresponds to

$$\begin{aligned} \bar{\xi} &:= (\bar{\sigma}, \bar{\phi}, \bar{v}, \bar{b}, \bar{q}, \bar{\tau}) \in \bar{\Xi}, \\ \bar{\Xi} &:= \{\bar{\xi} \in \mathbb{R}^3 \times \{-1, 1\} \times \{-1, 0, 1\} \times [0, 2\delta] : \\ &\quad \bar{q}\bar{v} \geq 0, \bar{b}\bar{q}\bar{\sigma} \geq 0, \bar{\sigma}\bar{\phi} \geq \frac{k_p}{k_i}\bar{\sigma}^2, \bar{b}\bar{q}\bar{\phi} \geq 0\}. \end{aligned} \quad (44a)$$

Note that, just as in the previous automaton (23), the sign of the new state variable \bar{q} is never opposite to the sign of \bar{v} , due to the constraints in $\bar{\Xi}$. Moreover, the timer $\bar{\tau}$ is constrained to evolve in the compact set $[0, 2\delta]$. The hybrid dynamics of the extended hybrid model \mathcal{H}_δ are

$$\mathcal{H}_\delta: \begin{cases} \dot{\bar{\xi}} = \bar{\mathcal{F}}(\bar{\xi}), & \bar{\xi} \in \mathcal{C}_{\text{slip}} \cup \mathcal{C}_{\text{stick}} \\ \bar{\xi}^+ \in \bar{\mathcal{G}}(\bar{\xi}), & \bar{\xi} \in \bigcup_{p \in \{\sigma, v, 0, 1, -1\}} \mathcal{D}_p. \end{cases} \quad (44b)$$

The flow and jump maps \mathcal{F} and \mathcal{G} of \mathcal{H}_δ are defined as

$$\bar{\mathcal{F}}(\bar{\xi}) := \begin{bmatrix} -k_i \bar{v} \\ \bar{\sigma} - k_p \bar{v} \\ -k_d \bar{v} + |\bar{q}| \bar{\phi} - \bar{q} (F_s - |\psi(\bar{v})|) \\ 0 \\ 0 \\ 1 - d z_1(\bar{\tau}/\delta) \end{bmatrix}, \quad (44d)$$

⁷Here, just as in Lemma 3, for any solution ξ we denote $j(t) = \min_{j \in \mathbb{Z}} \{j : (t, j) \in \text{dom } \bar{x}\}$.

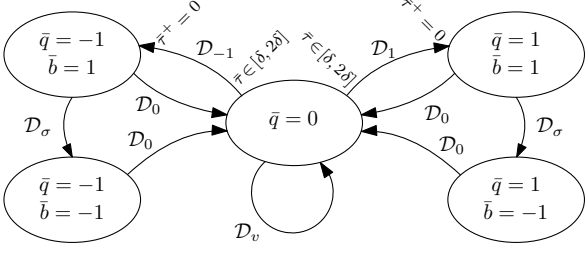


Figure 23: Hybrid-automaton illustration of (44).

$$\begin{aligned} \bar{\mathcal{C}}(\bar{\xi}) &:= \bigcup_{p \in \{\sigma, v, 0, 1, -1\}: \bar{\xi} \in \mathcal{D}_p} \{g_p(\bar{\xi})\}, \quad (44e) \\ g_\sigma(\bar{\xi}) &:= [\bar{\sigma} \quad -\bar{\phi} \quad \bar{v} \quad -\bar{b} \quad \bar{q} \quad \bar{\tau}]^\top, \\ g_v(\bar{\xi}) &:= \left[\bar{\sigma} \quad \frac{k_p}{k_i} \bar{\sigma} \quad \bar{v} \quad -\bar{b} \quad \bar{q} \quad \bar{\tau} \right]^\top, \\ g_0(\bar{\xi}) &:= [\bar{\sigma} \quad \bar{\phi} \quad \bar{v} \quad \bar{b} \quad 0 \quad \bar{\tau}]^\top, \\ g_1(\bar{\xi}) &:= [\bar{\sigma} \quad \bar{\phi} \quad \bar{v} \quad \bar{b} \quad 1 \quad 0]^\top, \\ g_{-1}(\bar{\xi}) &:= [\bar{\sigma} \quad \bar{\phi} \quad \bar{v} \quad \bar{b} \quad -1 \quad 0]^\top. \end{aligned}$$

The flow and jump sets of \mathcal{H}_δ are defined as

$$\begin{aligned} \mathcal{C}_{\text{slip}} &:= \{\bar{\xi} \in \bar{\Xi}: |\bar{q}| = 1\}, \\ \mathcal{C}_{\text{stick}} &:= \{\bar{\xi} \in \bar{\Xi}: \bar{v} = 0, |\bar{\phi}| \leq F_s, \bar{q} = 0\}, \\ \mathcal{D}_\sigma &:= \{\bar{\xi} \in \bar{\Xi}: \bar{\sigma} = 0, \bar{b} = 1, |\bar{q}| = 1\}, \\ \mathcal{D}_v &:= \{\bar{\xi} \in \bar{\Xi}: \bar{v} = 0, \bar{b} = -1, \bar{q} = 0\}, \quad (44f) \\ \mathcal{D}_0 &:= \{\bar{\xi} \in \bar{\Xi}: \bar{v} = 0, |\bar{q}| = 1\}, \\ \mathcal{D}_1 &:= \{\bar{\xi} \in \bar{\Xi}: \bar{v} = 0, \bar{\phi} \geq F_s, \bar{b} = 1, \bar{q} = 0, \bar{\tau} \in [\delta, 2\delta]\}, \\ \mathcal{D}_{-1} &:= \{\bar{\xi} \in \bar{\Xi}: \bar{v} = 0, \bar{\phi} \leq -F_s, \bar{b} = 1, \bar{q} = 0, \bar{\tau} \in [\delta, 2\delta]\}, \end{aligned}$$

Finally, based on (44f), we define

$$\bar{\mathcal{C}} := \mathcal{C}_{\text{slip}} \cup \mathcal{C}_{\text{stick}}, \quad \bar{\mathcal{D}} := \mathcal{D}_\sigma \cup \mathcal{D}_v \cup \mathcal{D}_0 \cup \mathcal{D}_1 \cup \mathcal{D}_{-1}. \quad (44g)$$

The different jump and flow sets are visualized, in Figure 22 by repeating the physical state variables for each value of the logical variable \bar{q} . Instead, Figure 23 shows the hybrid automaton representation of all the transitions enabled by the flow-jump mechanism of the hybrid dynamics. It is emphasized that the evolution of this Stribeck solution is significantly more complex than the one reported in Figure 9 for the Coulomb case.

Paralleling the result of Lemma 3, using the dwell time result of Lemma 6, it is possible to prove that \mathcal{H}_δ in (44) represents semiglobally the solutions to the reset-endowed hybrid closed-loop (39). This result, reported below, is taken from [18, Prop. 6] and enables carrying over the stability properties from (44) to (39). As in the previous results, with a slight abuse of notation we use a unified symbol $j(\cdot)$ to characterize $j(t) := \min_{(t,k) \in \text{dom } \psi} k$, even though this function depends on the domain of the solution under consideration (which is always clear from the context).

Lemma 7. *Under Assumption 2, for each compact set \mathcal{K} and the corresponding $\delta(\mathcal{K}) > 0$ characterized in Lemma 6, for each solution $\xi = (\sigma, \phi, v, b)$ to (39) with $\xi(0, 0) = \xi_0 \in \mathcal{K}$, there exist q_0, τ_0 and a solution $\bar{\xi} = (\bar{\sigma}, \bar{\phi}, \bar{v}, \bar{b}, \bar{q}, \bar{\tau})$ to (44) starting at $\bar{\xi}(0, 0) = (\xi_0, \bar{q}_0, \bar{\tau}_0)$, such that*

$$\begin{aligned} \sigma(t, j(t)) &= \bar{\sigma}(t, j(t)), \quad \phi(t, j(t)) = \bar{\phi}(t, j(t)), \\ v(t, j(t)) &= \bar{v}(t, j(t)), \quad b(t, j(t)) = \bar{b}(t, j(t)), \end{aligned} \quad (45)$$

for all $t \geq 0$ such that $\xi(t, j(t)) \notin \mathcal{A}_e$.

For the proof of Theorem 1 the use of the semiglobal hybrid representation (23) and the ensuing smooth Lyapunov function (27) was optional, due to the alternative proof technique of [22], which relies on the discontinuous Lyapunov-like function (25). Instead, for the proof of Theorem 3, exploiting the hybrid extended model (44) appears to be the only viable route. In particular, we illustrate in the next section a new Lipschitz hybrid Lyapunov function that generalizes the smooth function \bar{V} given in (27) and enjoys the necessary decrease properties for proving convergence of the solutions to (44). The proof of Theorem 3 then uses the representation result of Lemma 7.

6.5. Lyapunov function for proving Theorem 3

To the end of proving Theorem 3 by exploiting the properties of the hybrid extended model (44) and Lemma 7, a first step is to represent the attractor \mathcal{A}_e in (40) lifted in the new directions associated with the extended state $\bar{\xi}$.

To prove suitable stability properties of \mathcal{H}_δ in (44), we introduce the following lifting of the attractor \mathcal{A}_e in (40) as

$$\bar{\mathcal{A}}_e := \{\bar{\xi} \in \bar{\Xi}: \bar{\sigma} = \bar{v} = 0, \bar{\phi} \in F_s \text{Sign}(\bar{b}\bar{q})\}, \quad (46)$$

where the extra variables \bar{q} and $\bar{\tau}$ can be selected arbitrarily within the set $\bar{\Xi}$ as long as the consistency property $\bar{b}\bar{q}\bar{\phi} \geq 0$ is satisfied.

Focusing on the lifted attractor $\bar{\mathcal{A}}_e$, we may then introduce the locally Lipschitz Lyapunov function

$$\begin{aligned} \bar{V}_e(\bar{\xi}) &:= \begin{bmatrix} \bar{\sigma} \\ \bar{v} \end{bmatrix}^\top \begin{bmatrix} \frac{k_d}{k_i} & -1 \\ -1 & k_p \end{bmatrix} \begin{bmatrix} \bar{\sigma} \\ \bar{v} \end{bmatrix} + |\bar{q}|(\bar{\phi} - \bar{b}\bar{q}F_s)^2 \\ &+ (1 - |\bar{q}|)dz_{F_s}^2(\bar{\phi}) + 2\frac{k_p}{k_i}F_s(\bar{b}\bar{q}\bar{\sigma} + (1 - |\bar{q}|)|\bar{\sigma}|). \end{aligned} \quad (47)$$

Function \bar{V}_e is an extension of the smooth Lyapunov function \bar{V} in (27), where we added the last term inducing a desirable nonincrease property along the solutions with Stribeck friction. This property was not enjoyed by \bar{V} as partially illustrated by the top plot of the simulations in Figure 19.

The additional last term in \bar{V}_e is nonsmooth (but Lipschitz) because it involves the nonsmooth factor $|\bar{\sigma}|$. This factor can be dealt with in a Lyapunov decrease condition using the Clarke generalized gradient $\partial\bar{V}_e(y)$ of \bar{V}_e at y as discussed in [29, Ch. 2].

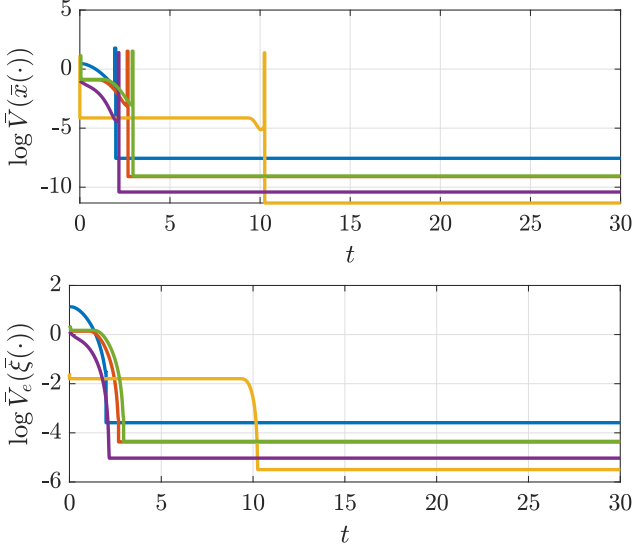


Figure 24: Evolution of the two functions \bar{V} and \bar{V}_e in (27) and (47), respectively, along the Stribeck solutions with reset compensation represented in Figure 21.

The next proposition establishes useful properties required of a hybrid Lyapunov function, that is, positive definiteness with respect to $\bar{\mathcal{A}}_e$ and radial unboundedness, non-increase along flow in $\bar{\mathcal{C}}$, and non-increase across jumps from $\bar{\mathcal{D}}$. This proposition parallels the previous result in Proposition 2 and establishes the key ingredient for the proof of the main result of [18], summarized in Theorem 3.

Proposition 4. *Under Assumption 2, the Lyapunov function \bar{V}_e in (47) is*

- (i) *positive definite with respect to $\bar{\mathcal{A}}_e$ in $\bar{\mathcal{C}} \cup \bar{\mathcal{D}}$ and radially unbounded relative to $\bar{\mathcal{C}} \cup \bar{\mathcal{D}}$;*
- (ii) *with $c := 2(k_p k_d - k_i) > 0$ as in Proposition 1, the Clarke directional derivative of \bar{V}_e along the flow dynamics of (44) satisfies*

$$V_e^\circ(\bar{\xi}) := \max_{\nu \in \partial V_e(\bar{\xi})} \langle \nu, \mathcal{F}(\bar{\xi}) \rangle \leq -c\bar{v}^2 \leq 0, \quad \forall \bar{\xi} \in \bar{\mathcal{C}};$$

- (iii) *for each $p \in \{\sigma, v, 1, -1, 0\}$, the jump dynamics of (44) satisfies*

$$\bar{V}_e(g_p(\bar{\xi})) - \bar{V}_e(\bar{\xi}) \leq 0, \quad \forall \bar{\xi} \in \bar{\mathcal{D}}_p.$$

Figure 24 provides an illustration of the Lyapunov decrease established in Proposition 4 by comparing the evolution of the smooth Lyapunov function $\bar{x} \mapsto \bar{V}(\bar{x})$ in (27) (where we recall that \bar{x} is a subcomponent of state $\bar{\xi}$) to the evolution of the Lipschitz Lyapunov function \bar{V}_e in (47) along the solutions already represented in Figure 21. We observe from the top plot of Figure 24 that function \bar{V} exhibits some increase during the time intervals just preceding a stick-to-slip transition (namely when $|\phi| \in [F_\infty, F_s]$

as emphasized in Section 6.1). Instead, function \bar{V}_e is always decreasing, confirming the result of Proposition 4. Note also that the logarithmic scale shows that the decrease of \bar{V}_e is not exponential, thereby opening the question for more advanced future solutions ensuring exponential convergence, rather than asymptotic convergence.

7. Experimental validation

In this section, we provide an experimental confirmation of the effectiveness of the proposed reset PID control solutions on an industrial high-precision motion stage. The stage represents a sample manipulation platform of an electron microscope (see [80]), and is depicted in Figure 25. The setup consists of a Maxon RE25 DC servo motor ① connected to a spindle ② via a coupling ③ that is stiff in the rotational direction while being flexible in the translational direction. The spindle drives a nut ④, transforming the rotary motion of the spindle to a translational motion of the attached carriage ⑤, with a ratio of $7.96 \cdot 10^{-5}$ m/rad. The position of the carriage is measured by a linear Renishaw encoder ⑥ with a resolution of 1 nm (and peak noise level of 4 nm). The desired position accuracy to be achieved is 10 nm, as specified by the manufacturer. For frequencies up to 200 Hz, the system dynamics can be well described by (4), where s represents the position of the carriage. The mass $m = 172.6$ kg consists of the transformed inertia of the motor and the spindle (with an *equivalent* mass of 171 kg), and of the mass of the carriage (1.6 kg).

The friction force for $\bar{\Psi}$ in (2) is mainly induced by the bearings supporting the motor axis and the spindle (see ⑦ and ⑧ in Figure 25), and by the contact between the spindle and the nut. The latter contact induces a significant Stribeck effect when lubricated and, if the spindle-nut contact is *not* lubricated, the setup shows dominantly static and viscous friction. In this way, the setup is an experimental platform for both the Coulomb and Stribeck cases (cf. Assumption 1 or 2) addressed in this paper, depending on the lubrication conditions and carriage position.

Remark 14. The friction characteristic in Figure 2 is experimentally obtained over the full stroke of the stage. We care to stress that the characteristic of Figure 2 only serves as a qualitative shape, as the friction is observed to be highly position-dependent, and dependent on the lubrication conditions of the spindle-nut contact. \lrcorner

For all the experiments (both with classical and reset PID controllers applied) the gains are selected as $\bar{k}_p = 10^7$ N/m, $\bar{k}_d = 2 \cdot 10^3$ (Ns)/m, and $\bar{k}_i = 10^8$ N/(ms). This selection is obtained by employing well-known loop-shaping design techniques often applied in the industry, and satisfies the assumption on the gains in Assumption 1 and 2. For all the experiments, a fourth-order reference trajectory is applied to the stage so that it moves by one millimeter in one second (according to standard operation of the

nano-positioning stage). The goal is to control the system towards a specified error accuracy of 10 nm, specified by the manufacturer.

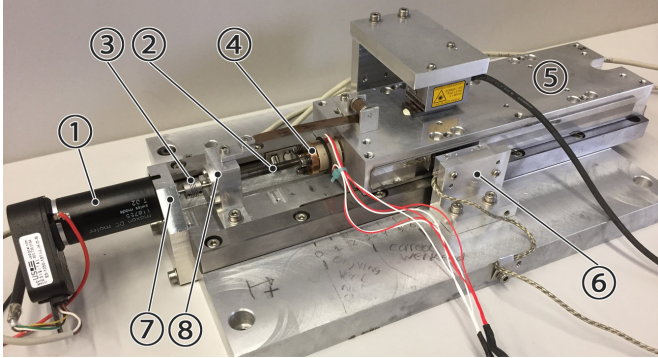


Figure 25: Experimental setup of a nano-positioning motion stage [17].

7.1. Coulomb friction case

For the Coulomb friction case, we experimentally compare the classical PID controller and the reset PID controller of Section 5 on transient performance, as reported in [17]. Namely, a motion system subject to Coulomb friction controlled by the classical PID controller suffers from poor transient performance and long settling times. The reset controller discussed in Section 5 is designed to significantly reduce the settling times by circumventing a large part of the depleting and refilling process of the integral buffer.

Despite the fact that the time regularization proposed in Section 5.2 avoids Zeno behavior, it is expected that, when the solution is close to the setpoint frequent and ineffective controller resets occur due to measurement noise. We therefore disable resets when the position error is within the desired accuracy band of 10 nm, i.e., if $|\sigma_o| \leq \bar{k}_i \cdot 10^{-8} \text{m} = 1 \text{ N/s}$ (cf. (31a)).

Consider Figure 26, which depicts the position error and corresponding scaled control force $\bar{u}/(4\bar{k}_i)$ for the classical PID controller and the reset PID controller, with different values for α . It can be observed that the reset controller results in shorter periods of stick and hence decreased settling times, compared to the classical PID controller. The results illustrate that, the larger the value for α , the shorter the settling times. For $\alpha = 1$, the system settles within the desired accuracy band 84% faster, compared to the classical PID case. Due to the low position error levels in the operating regime of the setup, microscopic frictional effects are non-negligible and affect the responses. In particular, frictional creep (see, e.g., [9, Ch. 2]), and some discontinuities are present in the position error response at controller reset instants due to frictional stiffness effects (see, e.g., [11, Sec. 2.1]). These effects are analyzed and discussed in more detail in [17, Sec. 5].

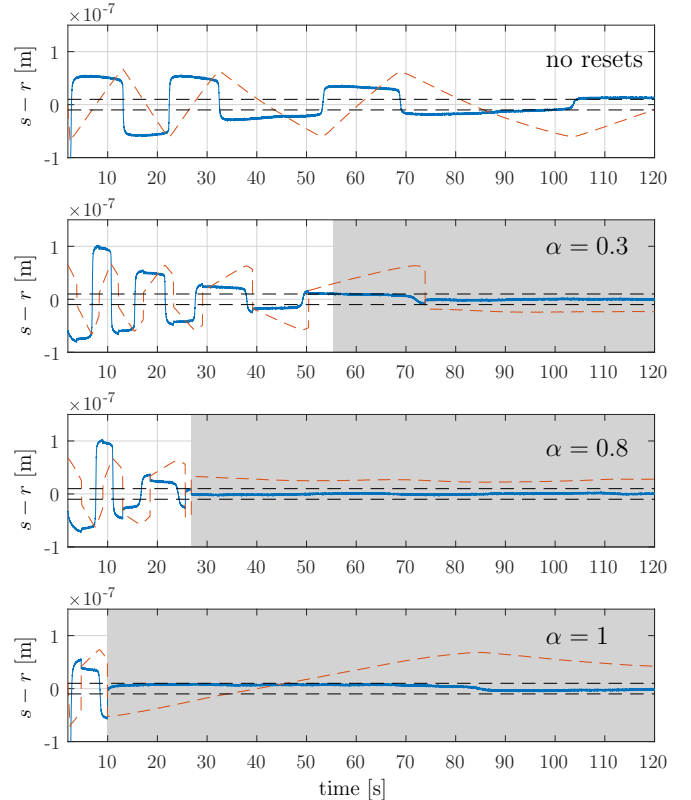


Figure 26: [17, Fig. 4] Position error (blue) and control force scaled by $4\bar{k}_i$ (red). The desired accuracy band is indicated by the black, dashed lines, which is reached at 56.7, 25.8, and 8.4 s for α equal to 0.3, 0.8, and 1, respectively, indicated by the gray patches.

7.2. Stribeck friction case

By lubricating the spindle-nut connection, and choosing a different carriage position, the setup suffers from a significant Stribeck effect. We now demonstrate experimentally the limitations of classical PID control, and the effectiveness of the reset PID controller of Section 6, as reported in [18].

Consider the top plot in Figure 27, which depicts the position response and control force scaled by $4\bar{k}_i$ for an experiment with the classical PID controller. Persistent oscillations are clearly visible, which prevent the system from settling within the desired accuracy band of 10 nm. We now apply the reset controller presented in Section 6, where we use the reset conditions in (41)-(42) to robustly detect zero crossings of the position error and the velocity. To avoid ineffective resets triggered by measurement noise (see also [18, Remark 1,2]), we disable resets as soon as the position error is within the desired accuracy band of 10 nm, after a reset from \mathcal{D}_v^f . After this reset, the integral control force is typically low so that the static friction yields robustness to other force disturbances. The resulting position error response and scaled control force are visualized in the lower plot of Figure 27. For comparative purposes, resets are enabled as soon as the PI control force and the position error have the same sign, after the first zero crossing of the position error (indicated by the

vertical dashed line). We observe that the system settles within the desired accuracy band after only two resets, in contrast to the response with the classical PID controller, thereby significantly improving the positioning accuracy. Due to the presence of microscopic frictional effects, overshoot is suppressed. A detailed analysis of the response at the nanometer scale can be found in [18, Sec. IV], as well as an analysis on the reset conditions.

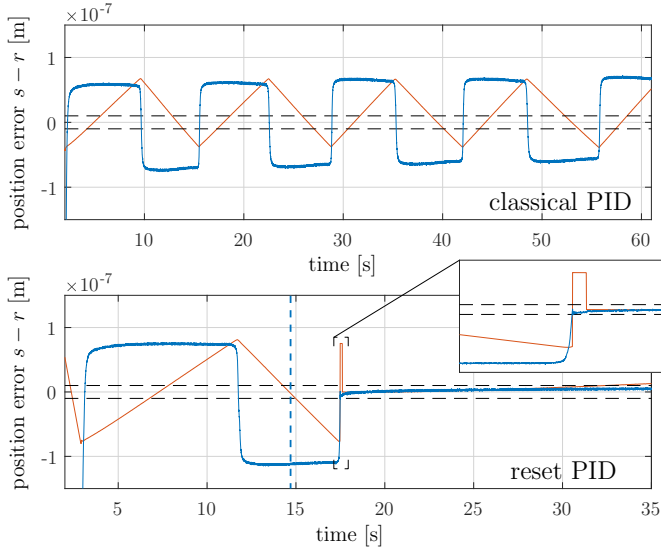


Figure 27: Position error (blue) and control force scaled by $4\bar{k}_i$ (red) for the classical PID controller (top plot) and reset PID controller (bottom plot). The desired accuracy band is indicated by the black, dashed lines.

7.3. Clegg reset solution for Stribeck friction

We report here on some additional results reported in [15, § 3.8], corresponding to the discussion given in Remark 12. In particular, we show experimentally that using a Clegg integrator solution resetting to zero x_c at the zero crossing of $s - r$ may result in a stabilizing action in the presence of Stribeck friction.

More specifically, we implement the following PID-based controller, where the linear integrator action of (5) is now replaced by the Clegg integrator [31] augmented with a dwell-time regularization, see [86, Eq. (8)-(10)], i.e.,

$$\begin{aligned} \begin{bmatrix} \dot{x}_c \\ \dot{\tau} \end{bmatrix} &= \begin{bmatrix} s - r \\ 1 - dz_1(\tau/\delta) \end{bmatrix}, \quad \text{with } (s - r)x_c \geq 0 \text{ or } \tau \in [0, \delta] \\ \begin{bmatrix} x_c^+ \\ \tau^+ \end{bmatrix} &= \begin{bmatrix} 0 \\ 0 \end{bmatrix}, \quad \text{with } (s - r)x_c \leq 0 \text{ and } \tau \in [\delta, 2\delta] \\ \bar{u} &= -\bar{k}_p(s - r) - \bar{k}_d v - \bar{k}_i x_c, \end{aligned} \quad (48)$$

with $\tau \geq 0$ is a timer variable. The integrator in (48) acts like a linear integrator whenever its input (i.e., the position error $s - r$) and state (i.e., x_c) have the same sign, and resets its state x_c to zero otherwise. A controller reset hence occurs only at a zero-crossing of $s - r$. The temporal regularization eliminates Zeno behavior, and, in

practice, avoids a chattering control signal by imposing that after any controller reset, at least a time interval of length $\delta > 0$ has to elapse before a subsequent reset is allowed.

The key mechanism for breaching persistent friction-induced oscillations by way of (48) is to prevent overcompensation of friction in the slip phase (subsequent to a stick phase). To this end, the control force acting on the system should decrease more than the friction force decrease caused by the velocity-weakening effect. For the specific experimental results reported here, we see experimentally that a sufficient decrease in control force is indeed obtained by the Clegg integrator (48). Although we leave as future work the investigation of sufficient conditions for proving rigorously the setpoint stability when using (48), we illustrate here the advantages of this solution. Among other things, the Clegg integrator is easier to implement as compared to the reset controller of Section 6 because it does not require a velocity measurements to detect the reset conditions.

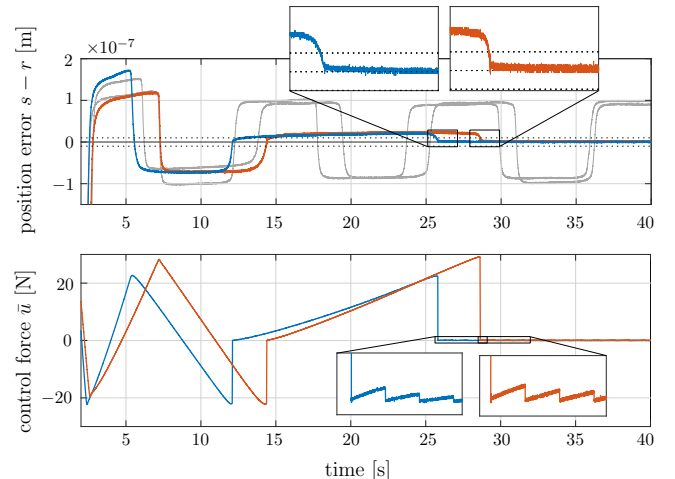


Figure 28: Position response for two experiments with the classical PID controller (gray), and position response and control force for two experiments with the Clegg reset controller (48) (blue, red).

Figure 28 reports on the experiments resulting from the Clegg reset controller (48) on our experimental setup. The gray curves show the persistent oscillations emerging when using the classical PID controller, as already demonstrated in Figure 27. Two experiments with the Clegg integral controller (48) have been performed and are visualized in blue and red color in the figure. In both cases, a classical integrator is active in the interval $[0, 10]$ and the Clegg solution is enabled after 10 s. Using the Clegg reset controller, the system consistently achieves a setpoint accuracy close to the noise level of the position measurements, and well within the specified accuracy band of 10 nm, after two resets. The lower subplot in Figure 28 shows the control force. The effect of resetting the integrator to zero upon a zero-crossing of $s - r$ is evident. Moreover, the dwell-time parameter τ avoids persistent controller resets when the

setpoint has been reached within the measurement accuracy, thereby avoiding a chattering control signal (see the insets in Fig 28). As the experimental results indicate, employing the Clegg integrator on a system with Stribeck friction may result in a high setpoint accuracy, in contrast to the classical PID controller. The essential insight is that a Clegg integrator realizes a sufficient reduction of the control force that counteracts the decrease in friction force caused by the Stribeck effect. Overcompensation of friction is thereby avoided.

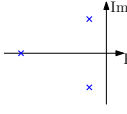
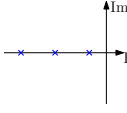
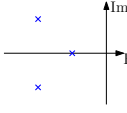
	k_p	k_i	k_d	Position	Eigenvalues
(a)	3	4	6.4		$-6.01, -0.19 \pm i0.79$
(b)	5.94	2.16	4.5		$-2.4, -1.5, -0.6$
(c)	11.4	5.4	4.6		$-2 \pm i2.24, -0.6$

Table 2: PID gains and corresponding eigenvalues of A in (17).

8. Results with different tuning of the PID gains

Throughout this paper we have considered the PID gains selection reported in Table 1, which are also reported as case (a) of Table 2. The motivation for this selection lies in the position of the eigenvalues of A illustrated in Table 2. In particular, typical industrial/experimental scenarios require fast rising time and, therefore, the rule of thumb for the PID gains tuning is to have one dominant pair of complex conjugate eigenvalues and a faster real eigenvalue. This configuration produces some overshoot and a fast rising time for the closed loop.

The goal of this section is to illustrate by simulations the fact that Assumptions 1 and 2, under which the reported results of Theorems 1–3 are valid, allow for more general selections of the PID gains. In particular, all that is required in our standing assumptions is that the PID gains lead to a Hurwitz matrix A in (17) (namely, all the eigenvalues of A have negative real part). This immediately suggests that two other relevant configurations may occur, one corresponding to three real eigenvalues (reported as case (b) in Table 2) and another one corresponding to a dominant real eigenvalue plus two faster eigenvalues that are complex conjugate (case (c) in Table 2).

For each one of those cases, we illustrate here a few simulation results providing a qualitative understanding of the responses to be expected with and without resets. The simulations that we show are to be compared against those reported in Figures 13 and 21 (see also Figure 16), and report the evolution of the three states $x = (\sigma, \phi, v)$,

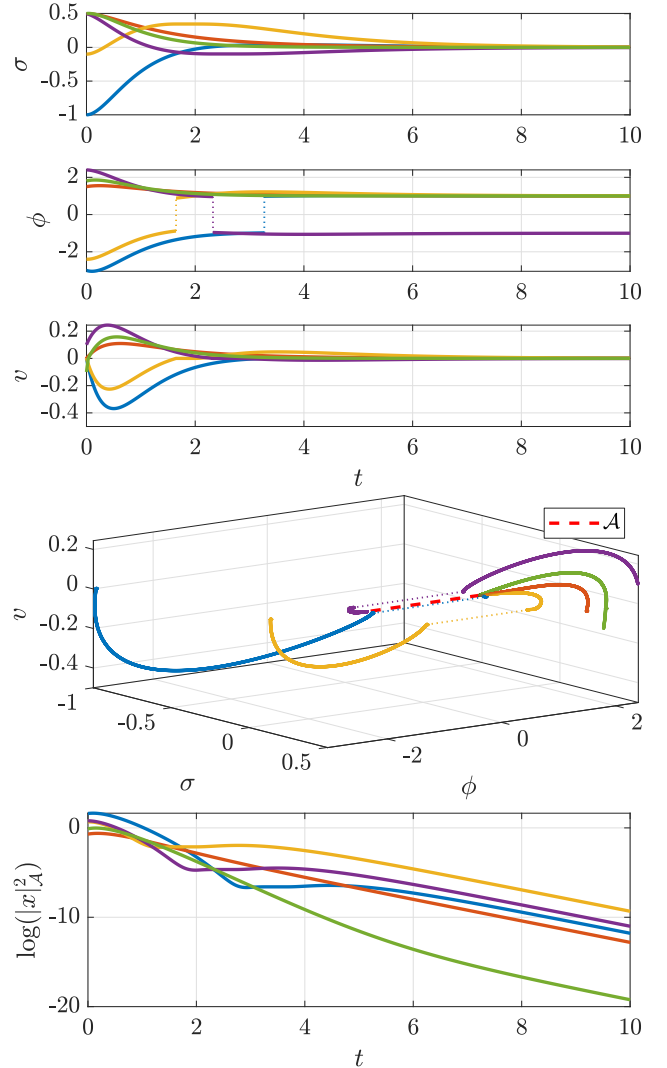


Figure 29: Responses of the reset PID closed loop (30) with Coulomb friction and the PID gains as in case (b) of Table 2.

together with the distance to the attractor (in logarithmic scale). A general conclusion from all the simulations carried out is that the action of our resetting laws enables re-establishing responses that are not too far from what one would expect based on the linear guidelines for PID tuning. This confirms that, also with resets, these specific PID gains selections do not lead to any evident advantage in terms of transient and steady-state response.

8.1. Case (b): three real eigenvalues

For the case of three real eigenvalues, we select the PID gains as reported in case (b) of Table 2. We expect in this case to see a non-overshooting response and therefore the solutions are expected to rarely enter a stick phase, this being the main reason why this configuration is undesired because it leads to a long settling time even for the linear response. The simulation results with Coulomb friction, represented in Figure 29, confirm this fact: only three of the considered solutions experience a jump (that is, enter

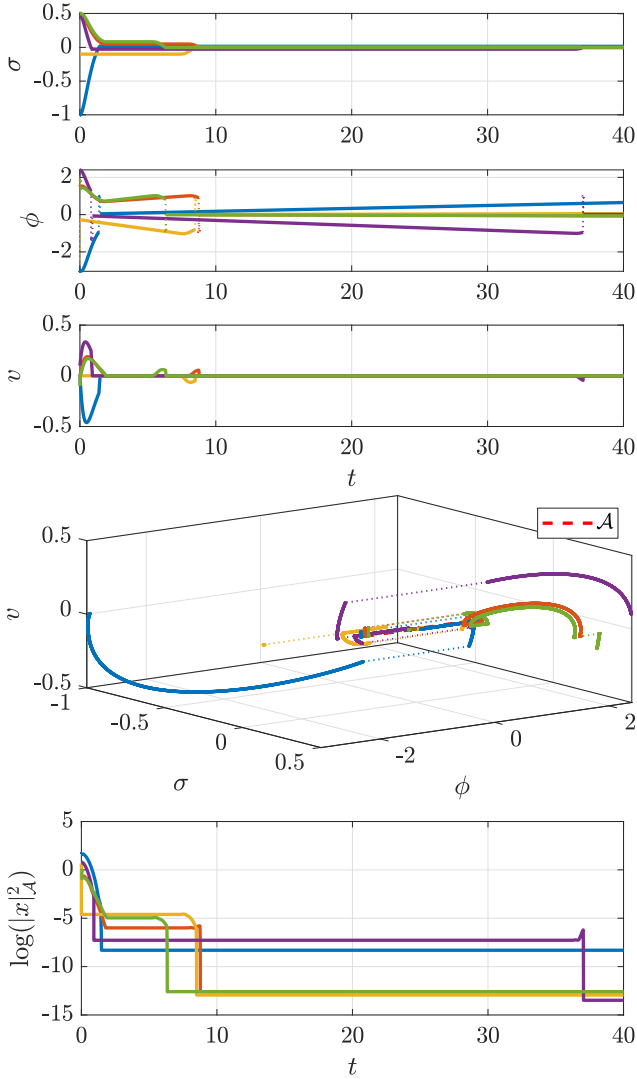


Figure 30: Responses of the reset PID closed loop (39) with Stribeck friction and the PID gains as in case (b) of Table 2.

a stick phase and trigger the reset action of our controller), and each one of those cases never resets again after that event. Inspecting the lower plot of Figure 29, which shows the distance to \mathcal{A} in logarithmic scale, we see that the solutions not performing jumps actually converge faster (and exponentially) to the attractor. The 3D plot also shows that the solutions converge to the two extremes of the attractor \mathcal{A} , which is reasonable when analyzing the evolution using the coordinate transformation proposed in Section 5.3.

The case with Stribeck friction is different and is reported in Figure 30. In this case, Theorem 3 establishes asymptotic stability of the attractor \mathcal{A}_e , therefore solutions are expected to converge asymptotically. By running simulations without reset actions, it is possible to inspect persistent oscillations, therefore instability of the attractor. As a consequence, for ensuring convergence, it is necessary that the solutions to the reset closed loop (39)

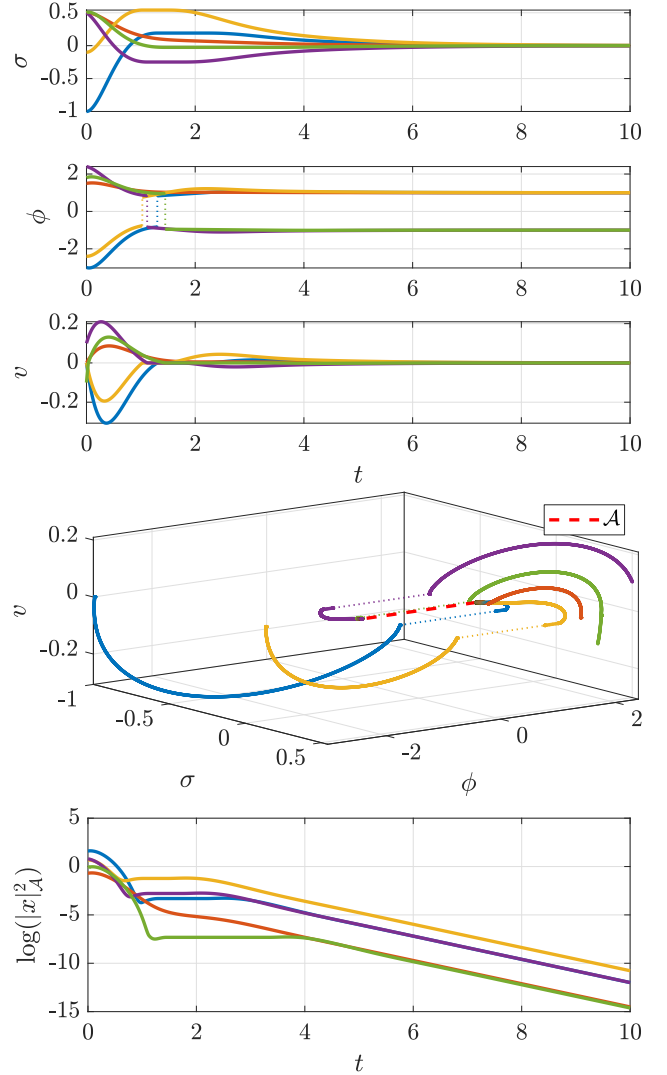


Figure 31: Responses of the reset PID closed loop (30) with Coulomb friction and the PID gains as in case (c) of Table 2.

keep jumping indefinitely. This is indeed the case when inspecting the curves of Figure 30. On the other hand, the lower plot of Figure 30, showing $|\xi|_{\mathcal{A}_e}^2 = |x|_{\mathcal{A}}^2$ in logarithmic scale, clearly indicates the fact that the convergence is not exponential because there is no linear upper bound on the logarithm of $|x|_{\mathcal{A}}^2$ (this fact becomes even more evident when running longer simulations).

8.2. Case (c): one real dominant eigenvalue

For the case of one real dominant eigenvalue and two faster complex conjugate ones, we select the PID gains as reported in case (c) of Table 2. This is a fairly unusual situation because linear solutions are expected to slowly converge to the setpoint while performing higher frequency oscillations. As a consequence we expect the solutions to enter stick phases without overshooting. This is indeed the case when looking at the Coulomb case reported in Figure 31. The figure reveals that some resets are triggered

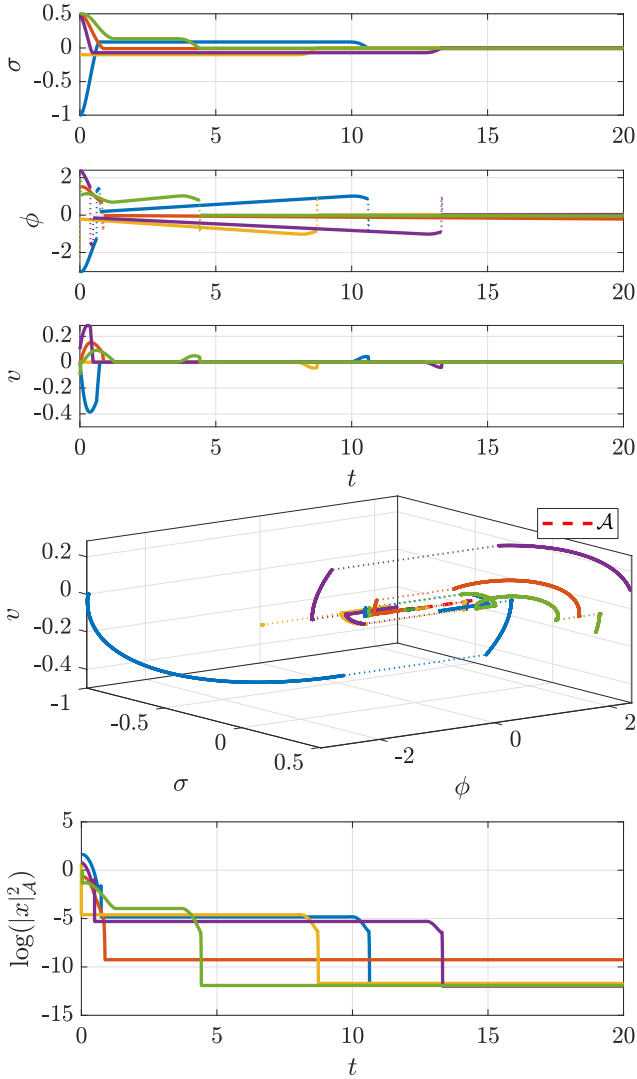


Figure 32: Responses of the reset PID closed loop (39) with Stribeck friction and the PID gains as in case (c) of Table 2.

by our law during the transient, but that once again none of the considered solutions jumps more than once, and the tail of the responses is purely linear and converges to one of the extremes of segment \mathcal{A} . Once again, the lower plot of Figure 31 shows that the convergence to \mathcal{A} is exponential due to the clear linear upper bound in logarithmic scale.

When considering the Stribeck scenario, the simulations without resets would again exhibit persistent oscillations around the setpoint. Figure 32 shows similar results to the previous case where resets are necessary to ensure convergence. Once again, the convergence to the attractor is not exponential, as illustrated by the lower plot of Figure 32.

9. Conclusions and future work

This review paper summarized a number of recent works providing reset control techniques for positioning systems

subject to Coulomb and Stribeck frictional effects. The proposed solutions, which are not based on the knowledge of the friction model, consist of a baseline PID control scheme augmented with resetting laws that address and resolve different drawbacks emerging with the nonlinear friction phenomena. The survey illustrated the importance of using Lyapunov theory and suitable closed-loop representations based on hybrid automata, logical variables and timers exploiting certain intrinsic semiglobal dwell time properties of the proposed closed loops. In the Coulomb case, we illustrated the improved transient responses in addition to showing exponential decay of a certain set of solutions. In the Stribeck case, the proposed solution resolves the well known instability (hunting phenomenon) associated to PID feedbacks. Simulation results have been used throughout the paper to well explain the rationale and the effect of the proposed reset laws. Moreover, experimental results on an industrial nano-positioning system have been reported to confirm the experimental relevance of the proposed solutions.

Future work includes providing a more rigorous proof of the exponential decay established in the conjecture reported in Section 5, in addition to providing revised and improved reset laws for the Stribeck case capable of inducing exponential convergence to zero of the error. Moreover, industrially relevant challenges comprise addressing the common case where the friction characteristic is not symmetric. As a matter of fact, while standard PID can cope with that problem, due to the internal model action embedded in the integral action, this is not the case for the proposed reset laws that require, so far, a symmetric friction model. Finally, specific assumptions will be investigated on the PID gains to obtain closed-loop guarantees with the simplified Clegg solution illustrated in Section 7.3.

References

- [1] W.H.T.M. Aangenent, G. Witvoet, W.P.M.H. Heemels, M.J.G. van de Molengraft, and M. Steinbuch. Performance analysis of reset control systems. *Int. J. of Robust and Nonlinear Control*, 20(11):1213–1233, 2010.
- [2] V. Acary and B. Brogliato. *Numerical Methods for Nonsmooth Dynamical Systems*. Springer, 2008.
- [3] L.T. Aguilar, Y. Orlov, and L. Acho. Nonlinear \mathcal{H}_∞ -control of nonsmooth time-varying systems with application to friction mechanical manipulators. *Automatica*, 39:1531–1542, 2003.
- [4] F. Al-Bender, V. Lampaert, and J. Swevers. The generalized Maxwell-slip model: a novel model for friction simulation and compensation. *IEEE Trans. Autom. Control*, 50(11):1883–1887, 2005.
- [5] F. Al-Bender and J. Swevers. Characterization of friction force dynamics. *IEEE Control Systems Magazine*, 28(6):64–81, 2008.
- [6] G. Amontons. De la résistance causée dans les machines. *Mémoires de L’Académie Royale des sciences*, pages 206–227, 1699.
- [7] A. Anthor, S. Zschaeck, and C. Ament. High precision position control using an adaptive friction compensation approach. *IEEE Trans. Autom. Control*, 55(1):274–278, 2010.
- [8] B. Armstrong and B. Amin. PID control in the presence of static friction: a comparison of algebraic and describing function analysis. *Automatica*, 32:679–692, 1996.

- [9] B. Armstrong-Hélouvy. *Control of machines with friction*. Springer, 1992.
- [10] B. Armstrong-Hélouvy and B. Amin. PID control in the presence of static friction. Technical Report EE-93-2, Dept. of Electrical Engineering and Computer Science, University of Wisconsin – Milwaukee, 1993.
- [11] B. Armstrong-Hélouvy, P. Dupont, and C. Canudas de Wit. A survey of models, analysis tools and compensation methods for the control of machines with friction. *Automatica*, 30(7):1083–1138, 1994.
- [12] A. Baños and A. Barreiro. *Reset control systems*. Springer, 2011.
- [13] G. Bartolini, A. Pisano, E. Punta, and E. Usai. A survey of applications of second-order sliding mode control to mechanical systems. *International Journal of Control*, 76:875–892, 2003.
- [14] G. Bartolini and E. Punta. Chattering elimination with second-order sliding modes robust to Coulomb friction. *Journal of Dynamic Systems, Measurement, and Control*, 122:679–686, 2000.
- [15] R. Beerens. *Reset Control and Control Allocation for High-precision Motion Systems*. PhD thesis, Eindhoven University of Technology, 2020. Available on https://pure.tue.nl/ws/portalfiles/portal/146206961/20200302_Beerens.pdf.
- [16] R. Beerens, A. Bisoffi, L. Zaccarian, W.P.M.H. Heemels, H. Nijmeijer, and N. van de Wouw. Hybrid PID control for transient performance improvement of motion systems with friction. In *Proc. 2018 American Control Conference*, pages 539–544, 2018.
- [17] R. Beerens, A. Bisoffi, L. Zaccarian, W.P.M.H. Heemels, H. Nijmeijer, and N. van de Wouw. Reset integral control for improved settling of PID-based motion systems with friction. *Automatica*, 107:483–492, 2019.
- [18] R. Beerens, A. Bisoffi, L. Zaccarian, H. Nijmeijer, W.P.M.H. Heemels, and N. van de Wouw. Reset PID design for motion systems with stibek friction. HAL, <https://hal.archives-ouvertes.fr/hal-02454405> and submitted for publication to the IEEE Transactions on Control Systems Technology, January 2020.
- [19] R. Beerens, H. Nijmeijer, W.P.M.H. Heemels, and N. van de Wouw. Set-point control of motion systems with uncertain set-valued Stribek friction. *IFAC PapersOnline*, 50(1):2965–2970, 2017.
- [20] O. Beker, C.V. Hollot, Y. Chait, and H. Han. Fundamental properties of reset control systems. *Automatica*, 40:905–915, 2004.
- [21] A. Bisoffi, R. Beerens, L. Zaccarian, W.P.M.H. Heemels, H. Nijmeijer, and N. van de Wouw. Hybrid model formulation and stability analysis of a PID-controlled motion system with Coulomb friction. In *Proc. 11th IFAC Symposium on Nonlinear Control Systems*, pages 84–89, 2019.
- [22] A. Bisoffi, M. Da Lio, A.R. Teel, and L. Zaccarian. Global asymptotic stability of a PID control system with Coulomb friction. *IEEE Trans. Autom. Control*, 63:2654–2661, 2018.
- [23] A. Bisoffi, F. Forni, M. Da Lio, and L. Zaccarian. Relay-based hybrid control of minimal-order mechanical systems with applications. *Automatica*, 97:104–114, 2018.
- [24] H. Brezis. *Opérateurs maximaux monotones et semi-groupes de contractions dans les espaces de Hilbert*. North Holland, 1973.
- [25] K. Camlibel, L. Iannelli, and A. Tanwani. Evolution inclusions with time-dependent maximal monotone operators. *arXiv preprint arXiv:1903.10803*, 2019.
- [26] C. Canudas De Wit, H. Olsson, and P.J.K. Lischinsky. A new model for control of systems with friction. *IEEE Trans. Autom. Control*, 40(3), 1995.
- [27] J. Carrasco and A. Baños. Reset control of an industrial in-line pH process. *IEEE Transactions on Control Systems Technology*, 20(4):1100–1106, 2012.
- [28] W. Chen, K. Kong, and M. Tomizuka. Dual-stage adaptive friction compensation for precise load side position tracking of indirect drive mechanisms. *IEEE Trans. on Control Syst. Technol.*, 23:164–175, 2015.
- [29] F.H. Clarke. *Optimization and nonsmooth analysis*. SIAM, Philadelphia, 1990.
- [30] E.M. Clarke Jr, O. Grumberg, D. Kroening, D. Peled, and H. Veith. *Model checking*. MIT Press, 2018.
- [31] J.C. Clegg. A nonlinear integrator for servomechanisms. *Transactions of the American Institute of Electrical Engineers, Part II: Applications and Industry*, 77(1):41–42, 1958.
- [32] P.R. Dahl. A solid friction model. Technical Report no. TOR-0158(3107-18)-1, Aerospace Corporation El Segundo, CA, 1968.
- [33] J.C.A. de Bruin, A. Doris, N. van de Wouw, W.P.M.H. Heemels, and H. Nijmeijer. Control of mechanical motion systems with non-collocation of actuation and friction: A Popov criterion approach for input-to-state stability and set-valued nonlinearities. *Automatica*, 45:405–415, 2009.
- [34] D.A. Deenen, M.F. Heertjes, W.P.M.H. Heemels, and H. Nijmeijer. Hybrid integrator design for enhanced tracking in motion control. In *Proc. 2017 American Control Conference*, pages 2863–2868, 2017.
- [35] F. Ferrante and L. Zaccarian. Dynamic reset output feedback with guaranteed convergence rate. In *Symposium on Nonlinear Control Systems (NOLCOS)*, pages 134–139, Vienna, Austria, September 2019.
- [36] F. Fichera, C. Prieur, S. Tarbouriech, and L. Zaccarian. Using Luenberger observers and dwell-time logic for feedback hybrid loops in continuous-time control systems. *International Journal of Robust and Nonlinear Control*, 23(10):1065–1086, 2013.
- [37] F. Fichera, C. Prieur, S. Tarbouriech, and L. Zaccarian. LMI-based reset \mathcal{H}_∞ design for linear continuous-time plants. *IEEE Transactions on Automatic Control*, 61(12):4157–4163, 2016.
- [38] A.F. Filippov. *Differential equations with discontinuous right-hand sides*. Kluwer Academic Publishers, 1988.
- [39] L. Freidovich, A. Robertsson, A. Shiriaev, and R. Johansson. LuGre-model-based friction compensation. *IEEE Trans. Control Syst. Technol.*, 18(1):194–200, 2010.
- [40] R. Goebel. A glimpse at pointwise asymptotic stability for continuous-time and discrete-time dynamics. In *Splitting Algorithms, Modern Operator Theory, and Applications*, pages 243–267. Springer, 2019.
- [41] R. Goebel, R.G. Sanfelice, and A.R. Teel. *Hybrid dynamical systems*. Princeton University Press, 2012.
- [42] R. Goebel and A. R. Teel. Preasymptotic stability and homogeneous approximations of hybrid dynamical systems. *SIAM review*, 52(1):87–109, 2010.
- [43] E. Haghverdi, P. Tabuada, and G.J. Pappas. Bisimulation relations for dynamical, control, and hybrid systems. *Theoretical Computer Science*, 342(2-3):229–261, 2005.
- [44] W.P.M.H. Heemels, G.E. Dullerud, and A.R. Teel. \mathcal{L}_2 -gain analysis for a class of hybrid systems with applications to reset and event-triggered control: A lifting approach. *IEEE Transactions on Automatic Control*, 61(10):2766–2781, 2016.
- [45] W.P.M.H. Heemels, V. Sessa, F. Vasca, and M.K. Camlibel. Computation of periodic solutions in maximal monotone dynamical systems with guaranteed consistency. *Nonlinear Analysis: Hybrid Systems*, 24:100–114, 2017.
- [46] R.H.A. Hensen, M.J.G. van de Molengraft, and M. Steinbuch. Friction induced hunting limit cycles: A comparison between the LuGre and switch friction model. *Automatica*, 39(12):2131–2137, 2003.
- [47] I. Horowitz and P. Rosenbaum. Non-linear design for cost of feedback reduction in systems with large parameter uncertainty. *International Journal of Control*, 21(6):977–1001, 1975.
- [48] L. Iannelli, K.H. Johansson, U.T. Jönsson, and F. Vasca. Averaging of nonsmooth systems using dither. *Automatica*, 42(4):669–676, 2006.
- [49] K.R. Krishnan and I.M. Horowitz. Synthesis of a non-linear feedback system with significant plant-ignorance for prescribed system tolerances. *Int. J. of Control*, 19:689–706, 1974.
- [50] R. I. Leine and H. Nijmeijer. *Dynamics and Bifurcations of Non-Smooth Mechanical Systems*. Springer Verlag, 2004.
- [51] R. I. Leine and N. van de Wouw. *Stability and convergence of mechanical systems with unilateral constraints*, volume 36. Springer Science & Business Media, 2008.
- [52] Y. Li, G. Guo, and Y. Wang. Reset control for midfrequency

- narrowband disturbance rejection with an application in hard disk drives. *IEEE Transactions on Control Systems Technology*, 19(6):1339–1348, 2011.
- [53] X. Lou, Y. Li, and R.G. Sanfelice. Robust stability of hybrid limit cycles with multiple jumps in hybrid dynamical systems. *IEEE Transactions on Automatic Control*, 63(4):1220–1226, 2018.
- [54] C. Makkar, G. Hu, W.G. Sawyer, and W.E. Dixon. Lyapunov-based tracking control in the presence of uncertain nonlinear parameterizable friction. *IEEE Trans. Autom. Control*, 52(10):1988–1994, 2007.
- [55] N. Mallon, N. van de Wouw, D. Putra, and H. Nijmeijer. Friction compensation in a controlled one-link robot using a reduced-order observer. *IEEE Trans. Control Syst. Technol.*, 14(2):374–383, 2006.
- [56] R. Milner. *Communication and concurrency*, volume 84. Prentice Hall, 1989.
- [57] G.J. Minty. Monotone (nonlinear) operators in Hilbert space. *Duke Mathematical Journal*, 29(3):341–346, 1962.
- [58] J.J. Moreau. Evolution problem associated with a moving convex set in a Hilbert space. *J. Differential Equations*, 26:347–374, 1977.
- [59] A. Morin. New friction experiments carried out at Metz in 1831–1833. *Proc. of the French Royal Academy of Sciences*, 4:1–128, 1833.
- [60] J. Na, Q. Chen, X. Ren, and Y. Guo. Adaptive prescribed performance motion control of servo mechanisms with friction compensation. *IEEE Trans. Ind. Electron.*, 61(1):486–494, 2014.
- [61] D. Nešić, A.R. Teel, and L. Zaccarian. Stability and performance of SISO control systems with first-order reset elements. *IEEE Trans. Autom. Control*, 56(11):2567–2582, 2011.
- [62] D. Nešić, L. Zaccarian, and A.R. Teel. Stability properties of reset systems. *Automatica*, 44(8):2019–2026, 2008.
- [63] H. Olsson, K. J. Åström, C. Canudas-de-Wit, M. Gäfvert, and P. Lischinsky. Friction models and friction compensation. *European Journal of Control*, 4(3):176–195, 1998.
- [64] Y. Orlov, R. Santiesteban, and L.T. Aguilar. Impulsive control of a mechanical oscillator with friction. In *Proc. American Control Conference*, pages 3494–3499, 2009.
- [65] F.S. Panni, H. Waschl, D. Alberer, and L. Zaccarian. Position regulation of an EGR valve using reset control with adaptive feedforward. *IEEE Transactions on Control Systems Technology*, 22(6):2424–2431, 2014.
- [66] G.J. Pappas. Bisimilar linear systems. *Automatica*, 39(12):2035–2047, 2003.
- [67] A.A. Pervozvanski and C. Canudas de Wit. Asymptotic analysis of the dither effect in systems with friction. *Automatica*, 38(1):105–113, 2002.
- [68] J. Peypouquet and S. Sorin. Evolution equations for maximal monotone operators: Asymptotic analysis in continuous and discrete time. *Journal of Convex Analysis*, 17(3&4):1113–1163, 2010.
- [69] G. Pola, A.J. van der Schaft, and M.D. Di Benedetto. Bisimulation theory for switching linear systems. In *IEEE Conference on Decision and Control*, pages 1406–1411, 2004.
- [70] C. Prieur, I. Queinnec, S. Tarbouriech, and L. Zaccarian. Analysis and synthesis of reset control systems. *Foundations and Trends in Systems and Control*, 6(2-3):117–338, 2019.
- [71] C. Prieur, S. Tarbouriech, and L. Zaccarian. Lyapunov-based hybrid loops for stability and performance of continuous-time control systems. *Automatica*, 49(2):577–584, 2013.
- [72] D. Putra, H. Nijmeijer, and N. van de Wouw. Analysis of undercompensation and overcompensation of friction in 1DOF mechanical systems. *Automatica*, 43(8):1387–1394, 2007.
- [73] D. Rijlaarsdam, P. Nuij, J. Schoukens, and M. Steinbuch. Frequency domain based nonlinear feed forward control design for friction compensation. *Mechanical Systems and Signal Processing*, 27(1):551–562, 2012.
- [74] M. Ruderman and M. Iwasaki. Analysis of linear feedback position control in presence of presliding friction. *IEEJ Journal of Industry Applications*, 5:61–68, 2015.
- [75] E. D. Sontag. An algebraic approach to bounded controllability of linear systems. *International Journal of Control*, 39(1):181–188, 1984.
- [76] R. Stribeck. Die wesentlichen Eigenschaften der Gleit- und Rollenlager. *Zeitschrift des Vereines Deutscher Ingenieure*, 46(38,39):1342–1348, 1432–1437, 1902.
- [77] J. Swevers, F. Al-Bender, C.G. Ganseman, and T. Prajogo. An integrated friction model structure with improved presliding behavior for accurate friction compensation. *IEEE Trans. Autom. Control*, 45(4):675–686, 2000.
- [78] S. Tarbouriech, T. Loquen, and C. Prieur. Anti-windup strategy for reset control systems. *Int. J. of Robust and Nonlinear Control*, 21(10):1159–1177, 2011.
- [79] A. R. Teel, F. Forni, and L. Zaccarian. Lyapunov-based sufficient conditions for exponential stability in hybrid systems. *IEEE Transactions on Automatic Control*, 58(6):1591–1596, 2012.
- [80] Thermo Fisher Scientific. <https://www.fei.com/products/>.
- [81] J.J. Thomsen. Using fast vibrations to quench friction-induced oscillations. *Journal of Sound and Vibration*, 228(5):1079–1102, 1999.
- [82] N. van de Wouw and R.I. Leine. Robust impulsive control of motion systems with uncertain friction. *Int. J. of Robust and Nonlinear Control*, 22:369–397, 2012.
- [83] A.J. van der Schaft. Equivalence of dynamical systems by bisimulation. *IEEE Transactions on Automatic Control*, 49(12):2160–2172, 2004.
- [84] S.J.L.M. van Loon, K.G.J. Gruntjens, M.F. Heertjes, N. van de Wouw, and W.P.M.H. Heemels. Frequency-domain tools for stability analysis of reset control systems. *Automatica*, 82:101–108, 2017.
- [85] S. Yang and M. Tomizuka. Adaptive pulse width control for precise positioning under the influence of stiction and Coulomb friction. *Journal of Dynamic Systems, Measurement, and Control*, 110(3):221, 1988.
- [86] L. Zaccarian, D. Nešić, and A.R. Teel. First order reset elements and the Clegg integrator revisited. In *Proc. of the American Control Conference*, pages 563–568, Portland (OR), USA, June 2005.
- [87] G. Zhao and C. Hua. Improved high-order-reset-element model based on circuit analysis. *IEEE Transactions on Circuits and Systems - II*, 64(4):432–436, April 2017.
- [88] G. Zhao, D. Nešić, Y. Tan, and C. Hua. Overcoming overshoot performance limitations of linear systems with reset control. *Automatica*, 101:27–35, 2019.